

Florida State University Libraries

Electronic Theses, Treatises and Dissertations

The Graduate School

2007

Water Electrolysis at the Thermodynamic Limit

Matthew D. Merrill



THE FLORIDA STATE UNIVERSITY

COLLEGE OF ARTS AND SCIENCES

WATER ELECTROLYSIS AT THE THERMODYNAMIC LIMIT

By

MATTHEW D. MERRILL

A Dissertation submitted to the
Department of Chemistry and Biochemistry
in partial fulfillment of the
requirements for the degree of
Doctorate of Philosophy

Degree Awarded:
Fall Semester, 2007

The members of the Committee approve the Dissertation of Matthew D. Merrill defended on December 12, 2006.

Robert C. Dougherty
Professor Directing Dissertation

Anjaneyulu Krothapalli
Outside Committee Member

Timothy M. Logan
Committee Member

Nancy L. Greenbaum
Committee Member

Kenneth A. Goldsby
Committee Member

Approved:

Joseph B. Schlenoff, Chair
Department of Chemistry and Biochemistry

Joseph Travis, Dean
College of Arts and Sciences

The Office of Graduate Studies has verified and approved the above name committee members.

This work is dedicated to my Father, who asked me to knock and then opened the door.
To anyone and everyone to whom this work will be of use.

ACKNOWLEDGEMENTS

I would first like to acknowledge my gratitude to my parents and brother. The older I get, the more I understand and value the blessings you have given me. To all my family, you have provided such strong and nurturing roots. Dani, my beautiful wife, your love and support is amazing. And to my friends, thank you too for helping to get me where I am today and preparing me for tomorrow.

I would also like to acknowledge my gratitude to my committee members. Dr Greenbaum gave me my first opportunity and has been a supporting friend ever since. Dr Logan took the time to give me a hard time and challenged me to become a stronger, better student. Dr Goldsby stepped up when I needed more committee members. Dr Krothapali was the progenitor of the project initiated the collaboration between departments. Dr Dougherty put a lot of time and energy into me and encouraged my creativity. He kept me balanced, focused, and working. I would also like to acknowledge my gratitude to Dr Greska, who listened to me and believed in my work.

I would like to acknowledge my gratitude to the Department of Chemistry and Biochemistry. Thank you for providing me with teachers and a place to experiment. Thanks for the job and the opportunity to teach. Thanks for the administrators, staff, and everyone else who did, fixed, and cleaned for me.

Finally, I would like to acknowledge my gratitude to the Sustainable Energy Science and Engineering Center. It was a great place to play with hydrogen. It was also a great place to go to with delightful people to talk to when I had been holed up solo in my lab for too long. Oh yeah, thanks for the financial support too!

TABLE OF CONTENTS

List of Tables	vii
List of Figures	viii
Abstract	x
1. INTRODUCTION	1
1.1 Problem Statement	1
1.2 Water Electrolysis	1
1.3 Thermodynamics of Water Equilibria	2
1.4 The Electrochemical Cell	6
1.5 Water Catalysis	10
1.6 Design of Water Catalysts	14
1.7 Previous Work	17
2. CURRENT METHODS	20
2.1 Cell set-up	20
2.2 Electrolyte and equilibria calculations	20
2.3 Cathodic electrodeposition conditions	21
2.4 Linear voltammetry scan	21
2.5 Cyclic voltammetry	22
2.6 Chrono coulometry	23
2.7 Chrono potentiometry	23
2.8 Electrochemical impedance spectroscopy techniques	23
2.9 Scanning electron microscopy	25
2.10 Powder X-ray crystallography	25
2.11 X-ray photoelectron spectroscopy	25
3. Results and Discussion	27
3.1 Catalytic kinetics and performance	27
3.2 Electrodeposition variables and catalyst optimization	27
3.3 Catalyst/electrolyte interaction	38
3.4 Impedance characterization	41
3.5 Catalyst chemical structure	51
4. CONCLUSIONS	56

4.1 Creating the catalysts	56
4.2 Electrochemical characteristics	59
4.3 Catalyst chemical structure	63
APPENDICES	65
A. Symbols, terms, and constants	65
B. Reactions and Reduction Potentials	67
REFERENCES	69
BIOGRAPHICAL SKETCH	76

LIST OF TABLES

2.1	Electrodeposition solution conditions	22
3.1	O ₂ evolution kinetic parameters	30
3.2	H ₂ evolution kinetic parameters	32
3.3	Fe ²⁺ vs Fe ³⁺ electrodeposition conditions	33
3.4	Spectator ion electrodeposition conditions	35
3.5	The order of electrodeposition solution preparation steps	37

LIST OF FIGURES

1.1	Pourbaix diagram of water	4
1.2	Electrolysis cell	7
1.3	Electrode processes	8
1.4	Reaction profile	12
1.5	Symmetry of the energy barrier	13
1.6	Previous work on oxygen evolution catalysts	19
2.1	Impedance vector	24
2.2	Equivalent circuit and Nyquist plot	25
3.1	Oxygen evolution Tafel plot	28
3.2	Hydrogen evolution Tafel plot	28
3.3	Oxygen evolution catalyst collection	30
3.4	Hydrogen evolution catalyst collection	31
3.5	Fe^{2+} vs Fe^{3+} for NiFe electrodeposition	33
3.6	The electrodeposition solution electrolyte	34
3.7	Electrodeposition spectator ions	35
3.8	Electrodeposition pH	36
3.9	The order of electrodeposition solution preparation steps	37
3.10	The electrodeposition power density	38
3.11	Kinetics with respect to KOH concentration	39
3.12	Cyclic voltammetry of the NiFe oxide	40

3.13 Morphology of the NiFe oxide	41
3.14 Stability of the NiFe oxide	42
3.15 Nyquist plots of the NiFe oxide	43
3.16 Phase diagram of NiFe oxide	44
3.17 Phase diagram of CoFe oxide	45
3.18 Phase diagram of NiCo oxide	46
3.19 Tafel plot of impedance current densities	47
3.20 NiFe oxide impedance deviation	48
3.21 CoFe oxide impedance deviation	49
3.22 NiCo oxide impedance deviation	49
3.23 NiFe oxide impedance transfer coefficients	50
3.24 True NiFe oxide Z_R and Z_I values	51
3.25 SEM of NiFe _(a) , NiFe _(b) and NiV oxides and Pt support	52
3.26 X-ray powder crystallography of NiFe oxide	53
3.27 XPS Ni $2p^{3/2}$ multiplet of the NiFe oxide catalyst	54
3.28 XPS Fe $2p^{3/2}$ multiplet of the NiFe oxide catalyst	54
3.29 XPS O $1s$ multiplet of the NiFe oxide catalyst	55
4.1 Total catalytic efficiency	57
4.2 Impedance wave distortion in linear and non-linear systems	63

ABSTRACT

Metal oxide catalysts for alkaline water electrolysis were created through cathodic electrodeposition and the deposition variables were explored. It was discovered that the use of ammonium electrolytes and higher current densities during deposition improved catalytic kinetic performance for the oxygen and hydrogen evolution reactions. A NiFe oxide catalyst was developed with a greater than 99 % ideal charge transfer coefficient for oxygen evolution and a NiV oxide catalyst was developed with a greater than 99.9 % ideal charge transfer coefficient. Combined, the NiFe and NiV catalysts catalyzed water electrolysis at greater than 99 % efficiency below 10 mA/cm². The NiFe oxide was characterized as being both highly conductive and highly disordered. NiFe, CoFe, and NiCo oxide oxygen evolution catalytic mechanisms were elucidated with electrochemical impedance spectroscopy. The relationship between the charge transfer coefficient of the Butler-Volmer model and the charge transfer resistance of electrochemical impedance spectroscopy was empirically demonstrated. The distortions of impedance on non-linear systems was demonstrated and discussed.

CHAPTER 1

INTRODUCTION

1.1 Problem Statement

Molecular hydrogen can be produced through water electrolysis to sustain a renewable hydrogen fuel economy. The price of hydrogen fuel relative to competing fuels or competing methods of hydrogen fuel production will ultimately dictate the utility of water electrolysis in a free market economy. The objective of this work was to develop and characterize economical catalysts for water electrolysis. The cost of catalysis is affected by the efficiency of catalysis, the materials and methods for creating the catalysts, and the durability of the catalysts. Executing the objective of this work included exploring and understanding: 1) the method of creating catalysts and the effect of the method's variables on catalytic kinetics, 2) the electrochemical and dynamic characteristics of the catalysts, and 3) the structural and compositional characteristics of the catalysts.

1.2 Water Electrolysis

A water electrolysis system converts water to molecular hydrogen and oxygen gasses. Energy is invested in the process of water electrolysis so that the O-H bonds of water are broken, or lysed with electricity. The invested energy works to concentrate electrons on the hydrogen atoms during water electrolysis so that hydrogen gas, H_2 , serves as an energy carrier. Hydrogen gas is a fuel because the energy stored in H_2 can be released at a later time by recombination with molecular oxygen abundant in the atmosphere. The energy released from the recombination of hydrogen fuel and molecular oxygen can be harnessed to perform work. The improvement of water electrolysis is therefore important for the implementation of an economical and renewable hydrogen fuel economy.

Hydrogen fuel is commonly regarded as the best potential substitute for fuels derived from petroleum products. The desire for a hydrogen-based fuel economy is frequently cited as a result of an increasing awareness of the limitations of petroleum reserves combined with increasing demand for fuel and energy worldwide. There is also an apparent increase in awareness and concern about the effects of pollution and global warming resulting from the combustion of carbon-based fuels. In contrast to fossil fuels, the only byproduct of recombining hydrogen fuel with molecular oxygen is water.

The equilibrium of water with molecular oxygen is a fundamental chemical feature in biological and global systems. Water covers approximately 70 % of the earth’s surface and molecular oxygen composes 20 % of the troposphere [1]. The evolution of water oxidation in photosynthesis transformed the earth’s surface from an anaerobic to an aerobic environment some 3 billion years ago [1]. The evolution of O_2 from water is by far the primary mechanism by which energy is biologically fixed [1]. Photosynthetic production of molecular oxygen stores energy in biological electron carriers such as NADPH, which can be considered a biochemical functional equivalent to H_2 . The oxidation of H_2O to O_2 serves as a source of protons and electrons for the synthesis of other fuels such as NH_3 or CH_3OH .

The atmospheric content of O_2 can be used as an indicator for the energy budget of Earth’s biosphere. The approximately first-order increase in atmospheric O_2 through Earth’s history was the result of the biosphere’s capacity to fix energy from the sun [2]. A rational design of an energy infrastructure capable of sustainable human development would use the same equilibria as the Earth’s biosphere. An energy infrastructure that utilizes hydrogen fuel produced from water electrolysis with renewable energy would be biologically compatible.

1.3 Thermodynamics of Water Equilibria

The nature of the electrochemical equilibria of water, H_2O , with molecular hydrogen, H_2 , and molecular oxygen, O_2 , provides a useful system in which energy can be stored with water electrolysis or released with fuel cells. The two half-reactions that define water’s domain of electrochemical stability are given by equations 1.1 and 1.2. Half-reaction equations are written as reduction reactions by convention. The standard state reduction potentials are denoted with “°” and are given for 1.1 and 1.2. The standard state refers to conditions at room temperature (25 °C or 298 °K) and where all reactant and product concentrations are 1 M for solutions and 1 atm for gasses. An electrochemical cell utilizes a reductive half-

reaction on the cathode and an oxidative half-reaction on the anode. The standard state cell potential, E_{cell}° , is the difference between the standard cathodic electric potential, $E_{cathode}^{\circ}$, and the standard anodic electric potential, E_{anode}° , according to equation 1.3.



$$E_{cell}^0 = E_{cathode}^0 - E_{anode}^0 \quad (1.3)$$

Experimental conditions rarely correspond to the standard state with regards to pH, temperature, or reactant and product concentrations. The Nernst equation 1.4 is used for calculating non-standard state reaction potentials, E , where n is the number of electrons transferred per reaction, R is the gas law constant ($8.3145 \frac{\text{J}}{\text{mol}\cdot\text{K}}$), F is Faraday's constant ($9.6485 \times 10^4 \frac{\text{C}}{\text{mol}}$), T is temperature in kelvins, and K is the equilibrium constant. The equilibrium constant, K , for a given temperature is determined by the ratio of product and reactant concentrations as described by equation 1.5 when the rate at which reactants are converted to products is equal and opposite to the rate at which products are converted back to reactants. The Nernst equation is valuable because concentrations can be readily measured and used to calculate the minimum potential energy at which a reaction can proceed for non-standard states. Equations 1.6 and 1.7 are derived from the Nernst equation to calculate the reduction potentials for non-standard state concentrations and/or pressures water electrolysis reactions.

$$E = E_0 - \frac{RT\ln(K)}{nF} \quad (1.4)$$

$$K = \frac{[\text{products}]}{[\text{reactants}]} \quad (1.5)$$

$$E_{\text{O}_2}^{\circ} = 1.228\text{V} - 0.0592 \cdot \text{pH} + 0.0147 \cdot \log[\text{pO}_2] \quad (1.6)$$

$$E_{\text{H}_2}^{\circ} = 0.000\text{V} - 0.0591 \cdot \text{pH} - 0.0295 \cdot \log[\text{pH}_2] \quad (1.7)$$

All reduction potential equations in this work were taken from Pourbaix's Atlas of Electrochemical Equilibria in Aqueous Solutions [3]. A Pourbaix diagram illustrates the reduction potentials with respect to pH for a collection of reactions pertaining to a particular element or set of compounds. Pourbaix diagrams consider 1 M (or atm) products or reactants at standard state temperature and pressure unless otherwise noted. A Pourbaix

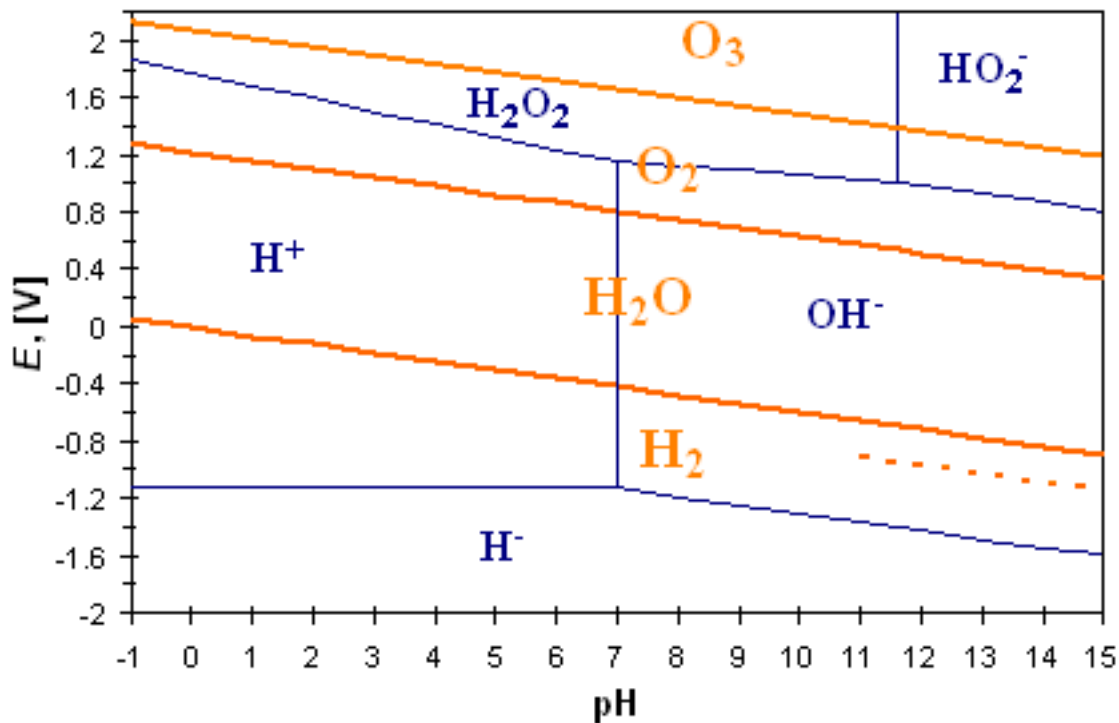


Figure 1.1: A Pourbaix diagram of water. The dashed line indicates the potential for alkaline hydrogen evolution according to water's ΔH_f .

diagram illustrating the electrochemical equilibria of water is presented in Figure 1.1. The electrochemical equilibria of water with the hydride ion, H^- , hydrogen peroxide, H_2O_2 , and ozone, O_3 , are also included in Figure 1.1. Note that the hydrogen and oxygen evolution reactions require the smallest negative and positive electric potentials, respectively, to perform redox chemistry on water. Other relevant standard half-reactions and potentials can be found in Appendix B.

The change in free energy, ΔG , of a reaction is the amount of work associated with the reaction. A reaction with a $-\Delta G$ is spontaneous and can do work by releasing energy. A reaction with a $+\Delta G$ is non-spontaneous and work must be done for the reaction to proceed. Spontaneity confers no meaning with respect to how fast the reaction will happen. ΔG is related to E according to equation 1.8. ΔG is also related to K according to equation 1.9. A water electrolysis cell is non-spontaneous and operates at a negative voltage potential because the reactions require the addition of free energy ($\Delta G > 0$). A fuel cell is spontaneous

($\Delta G < 0$) and operates at a positive voltage potential because the reactions release net free energy.

$$\Delta G^\circ = -nFE^\circ \quad (1.8)$$

$$\Delta G^\circ = -RT \ln(K) \quad (1.9)$$

The heat of water's formation (also known as the higher heating value), ΔH_f , is -1.481 V and is the minimum electric potential required for water electrolysis at standard state [4], [5], [6]. The free energy of formation (also known as the lower heating value), ΔG_f , is 1.228 V and is the maximum operating electric potential of a fuel cell at standard state. The difference in potential is explained with the Gibbs equation (1-10). Equation 1.10 includes the energy values for liquid water at room temperature (298 °K) according to equation 1.11. The entropic energy described by the $T\Delta S$ term is favorable for water electrolysis and may be contributed from the reaction environment. It is however kinetically faster to obtain energy for the $T\Delta S$ term from electrical energy than from the reaction environment's heat energy at room temperature. Practical rates of water electrolysis therefore require water's heat of formation (ΔH_f) potential rather than the free energy of formation (ΔG_f) potential. The -0.253 V of the $T\Delta S$ term occurs on the hydrogen evolution reaction at high pH and on the oxygen evolution reaction at low pH. Equation 1.12 considers the heat of water formation, ΔH_f , rather than the free energy of formation, ΔG_f , for the alkaline hydrogen evolution reaction and is indicated with the dashed line in Figure 1.1.

$$\Delta G(-237.192 \frac{\text{kJ}}{\text{mol}}) = \Delta H(-285.840 \frac{\text{kJ}}{\text{mol}}) - T \Delta S(48.648 \frac{\text{kJ}}{\text{mol} \cdot \text{K}}) \quad (1.10)$$



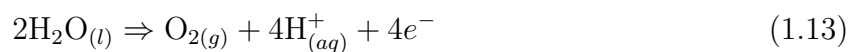
$$E_{\text{H}_2}^0 = 1.228\text{V} - 0.0592 \cdot \text{pH} - 1.481\text{V} - 0.0295 \cdot \log[\text{pH}_2] \quad (1.12)$$

Efficiency of water electrolysis can be represented by comparing power against current density because efficiency decreases at greater current densities. Power, P , has units in watts and is the product of current and voltage. In some cases it may be more appropriate to express efficiency as a quantity of hydrogen fuel per cost or kWh/kg H_2 . Electricity is commonly sold by the kilowatt hour (kWh) and hydrogen fuel is best quantified with kilograms (kg) because a mass of hydrogen does not require consideration of temperature, pressure, or phase. A kilogram of hydrogen fuel has approximately the same energy content

as a gallon of gasoline. Ideal efficiency for water electrolysis is calculated to be $39.39 \frac{\text{kWh}}{\text{kg H}_2}$ according to water's heat of formation (ΔH_f).

1.4 The Electrochemical Cell

An electrochemical cell combines an oxidation and a reduction reaction in mass and charge balance. The oxidation half-reaction occurs at the anode and removes electrons from a reactant substrate. The reduction half-reaction occurs at the cathode and donates electrons to a reactant substrate. Equation 1.13 is the oxidation (oxygen evolution) reaction and equation 1.14 is the reduction (hydrogen evolution) reaction of water electrolysis. Equation 1.14 has been multiplied through by a factor of two so that the combination of equations 1.13 and 1.14 are balanced according to mass and charge. Equation 1.15 represents the net water electrolysis cell reaction.



A water electrolysis cell is illustrated in Figure 1.2. The cell features the anode and cathode electrodes connected in a circuit to a power supply. An electrochemical workstation is a power supply capable of controlling and measuring both current and voltage in a variety of electrochemical methods. Only the difference in voltage between the anode and the cathode can be measured in a two-electrode system. A reference electrode is a third electrode that is required to specifically measure the voltage just for the electrode of interest. In a three-electrode system, the electrode being measured by the reference electrode is the working electrode and the remaining electrode is the counter electrode.

The electrodes are immersed in an electrolyte. The electrolyte contains mobile ions so that the electrolyte can conduct an ionic current. In water electrolysis, the conduction of an ionic current of positively charged protons through the electrolyte is necessary to establish charge neutrality as negatively charged electrons are moved from the anode to the cathode through the circuit wires. A strong electrolyte is desired because greater dissociation of the solute ions in a liquid electrolyte results in greater electrical conductivity. A solid polymer electrolyte is a membrane that specifically conducts protons but is impermeable to H_2 and O_2

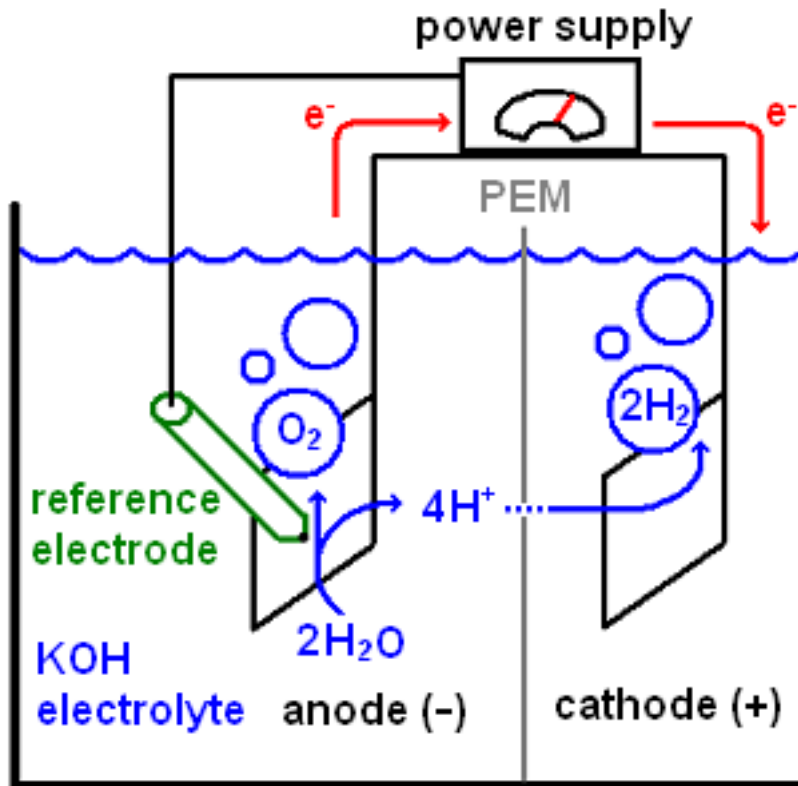


Figure 1.2: Schematic of a water electrolysis cell.

gasses is known as a proton exchange membrane (PEM) and is commonly used in complete water electrolysis and fuel cell systems.

The conductivity of an electrolyte is a function of ionic concentration, ionic mobility, and temperature. Group 1A and 2A metal hydroxides are strong bases, of which KOH has the greatest solubility and ionic mobility in water ($K^+ : 7.62 \times 10^{-8} \frac{m^2}{V \cdot s}$, $OH^- : 20.50 \times 10^{-8} \frac{m^2}{V \cdot s}$ [7]. The conductivity of KOH solutions depends upon temperature and concentration [8]. Even a strong base such as KOH does not completely dissociate in water and so the inclusion of ionic activity coefficients is required for calculating small but significant ionic dissociation effects upon pH. Vera *et al.* reports the actual pH of 1 M KOH to be 13.84 [9]. A literature survey of catalysts for alkaline water electrolysis indicated that a 1 M KOH electrolyte at room temperature and pressure was the most common experimental condition [10], [11], [12], [13], [14], [15], [16], [17], [18], [19], [20], [21], [22], [23].

Processes in an electrochemical cell, such as the conduction of ions in the electrolyte

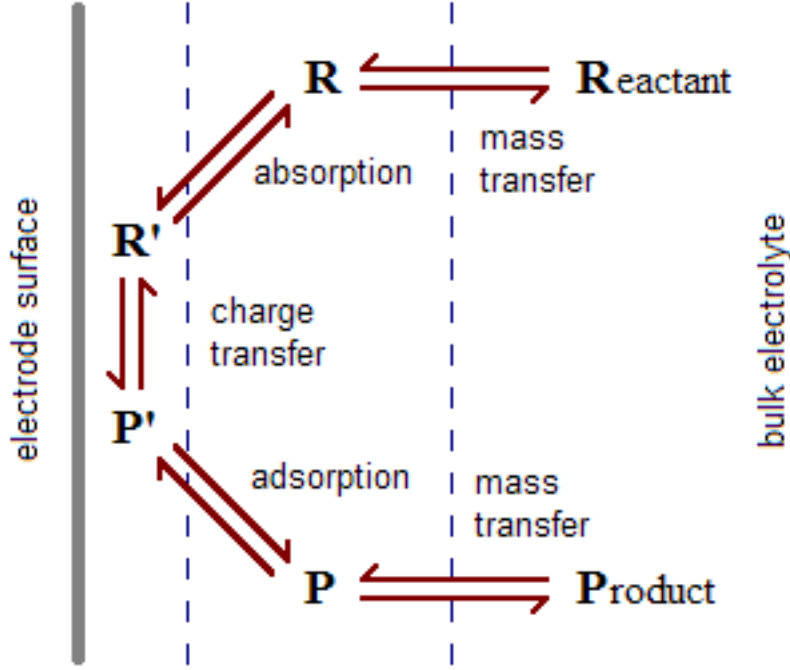


Figure 1.3: Chemical processes involved in an electrochemical cell.

and electron transfer reactions, contribute to losses in cell efficiency. The chemical processes relevant to this work are illustrated in Figure 1.3. These chemical processes contribute resistances that increase the voltage required to drive water electrolysis cells and decrease the voltage produced in fuel cells. Ohm's law describes the relationship of resistance, R , current, I , and electric potential, E , according to equation 1.16 where resistance has units in ohms. Energy losses in an electrochemical cell are due to mass transfer resistance, solution resistance, charge transfer resistance, and circuit resistance. Circuit resistance encompasses the resistances caused by the electrical wires and connections. Circuit resistances are eliminated by calibration of the electrochemical workstation and are not considered further in this work.

$$V = I \times R \quad (1.16)$$

The transfer of mass between electrodes that is faster than the mass's rate of diffusional flux causes mass transfer resistance. The conduction of protons through electrolyte and the bubbles of molecular H_2 and O_2 cause mass transfer resistance in water electrolysis

and fuel cells. The electrolyte conductivity, including membranes and salt bridges, spacing between electrodes, and void fractions caused by bubbles affect mass transfer resistance [24]. Experimental setups with the tip of the reference electrode in contact with the working electrode surface do not measure the mass transfer resistance.

Both the anodic and cathodic reactions have their own charge transfer resistances and solution resistances. Reactions at the interface between the electrode surface and the electrolyte cause solution resistances. Surface reactions include the absorption and adsorption of reactants and products onto the catalyst. Solution resistance is a function of the availability of both catalytic sites and reactants. A catalyst with a high surface area and a high concentration of active catalytic sites will have a minimal solution resistance. The presence of a water molecule may not be sufficient to serve as a reactant if the activity of the catalytic site is pH dependant. A linear increase in voltage corresponds to a linear increase in current when the solution resistance dominates the kinetics in the electrochemical cell.

The oxidation and reduction reactions at the electrodes cause charge transfer resistances. The charge transfer resistances include the transfer of nuclei (i.e. O and H) as well as electrons. The oxidation and reduction reactions have an ideal, minimal charge transfer resistance that is a function of the number of electrons transferred, temperature, and Boltzmann’s distribution. Non-ideal catalysts have additional charge transfer resistance when the energy required for electron and nuclear rearrangement is not conserved during catalysis causing the extra loss of energy as heat. Charge transfer resistance is quantified with charge transfer coefficients and will be discussed more thoroughly with regards to the Butler-Volmer model of electrode kinetics.

A working electrode demonstrates capacitance in addition to the resistances discussed above. The working electrode builds up a surface charge in proportion to the applied voltage and so the system has the characteristics of a capacitor. Capacitance, C , has units of farads, F , and equals 1 C/V . The capacitance at an electrode surface is commonly characterized as an electrical double layer. The double layer refers to the inner and outer Hemholtz planes. The inner Hemholtz plane contains electrolyte molecules or ions specifically absorbed onto the electrode surface. The outer Hemholtz plane contains electrolyte molecules or ions that are not specifically absorbed but whose orientations are affected through long-range electrostatic forces.

A change in applied potential causes a change in capacitance on the electrode surface

with a capacitive current. The capacitive current is dependent upon the velocity of the changing potential and the surface morphology of the electrode. A more rugged surface morphology causes a greater capacitive current because of a greater true-to-geometric surface area ratio. Cyclic voltammetry techniques can be used to characterize surface morphology of an electrode by scanning through a range of potential velocities. The cyclic voltammetry technique discussed by Da Silva *et al.* determines the difference between the differential capacitance, C_d , and the external differential capacitance, $C_{d,e}$ [25]. C_d is the total capacitance for all binding sites of the electrode surface while the $C_{d,e}$ only includes capacitance of the outermost binding sites that are accessible to the electrolyte at all potential velocities. $C_{d,i}$ is the internal differential capacitance and is the difference between C_d and $C_{d,e}$. $C_{d,i}$ only includes the binding sites deep within pores and cracks that are accessible to the electrolyte at low potential velocities but not at higher velocities. The morphology factor, φ , is the ratio of the internal and total capacitances according to equation 1.17 and characterizes the roughness of the electrode surface.

$$\varphi = \frac{C_{d,i}}{C_d} \quad (1.17)$$

1.5 Water Catalysis

A catalyst is a compound that increases the rate of a chemical reaction without being consumed in the process. The catalysts developed in this work are specifically known as electrocatalysts. An electrocatalyst mediates a reaction on an electrode surface so that a net flux of electrons is generated in an electrical circuit. In addition to catalyzing a reaction, the function of an electrocatalyst is to efficiently convert between chemical and electrical energy. The catalysts developed in this work are also referred to as a heterocatalyst because solid phase metal oxide is catalyzing water molecules in the liquid phase.

An ideal catalyst is efficient, selective, and durable. A turnover frequency or number is typically used to characterize the efficiency of a catalyst by quantifying the reaction rate. The reaction rate of an electrocatalyst is measured with a current density. The selectivity of a catalyst refers to the relative production of desired products to the production of byproducts. Durability reflects the lifetime of a catalyst, which is often measured as an average number of catalytic cycles performed before the catalyst becomes passive. Some catalysts are capable of being reformed or re-activated for re-use after becoming passive.

The Arrhenius equation 1.18 describes how the rate of a reaction, k , is dependent upon a frequency factor, A , the energy of activation, E_a , and temperature, T , in kelvins. The frequency factor is a function of the frequency of molecular collisions and the probability of the molecules colliding in a favorable orientation. The E_a is a potential energy barrier that represents the minimum energy required for a reaction to proceed. A catalyst can increase the rate of a reaction by either a) increasing the probability of a favorable collision, or b) lowering the energy of activation.

$$k = Ae^{\frac{E_a}{RT}} \quad (1.18)$$

The effect of a catalyst on the progress of a reaction is illustrated in Figure 1.4. A reaction must have a negative free energy in order to proceed in the forward direction. The E_a of an uncatalyzed reaction (A) may be large and the kinetics will be correspondingly slow. A catalyst can provide an alternate reaction mechanism through which the reaction can proceed. A smaller activation energy, E_a' , provided by the catalyzed pathway (B) will cause the reaction to proceed faster. Less energy is required to overcome smaller activation barrier and so less energy is lost as heat. The catalytic mechanism may be composed of more than one step and the overall rate of the reaction is limited by the slowest step, which would be the step with the largest E_a . The free energy of each step must also be negative in order for the reaction to proceed. A stable, unproductive complex will form between the catalyst and reaction intermediate if a step has a positive free energy as illustrated by pathway C.

The semi-classical Butler-Volmer model describes how the reaction energy barrier affects the relationship of current with respect to working potential near the equilibrium potential. The α value is the charge transfer coefficient and the J_0 value is the exchange current density. Equation 1.19 considers both the forward and reverse rates of an equilibrium where the exponential terms containing α_c and α_a values correspond to the cathodic and anodic currents, respectively. E is the applied working potential and E_0 is the midpoint potential so the difference, $E - E_0$, is the overvoltage for the working electrode. The number of electrons, n , is 4 for the oxygen evolution reaction and 2 for the hydrogen evolution reaction. Equations 1.20 and 1.21 are derived from 1.19 to describe reduction and oxidation reactions, respectively, in which the reverse current is assumed negligible.

$$\equiv J = J_0 \cdot \left[e^{\left[\frac{-\alpha_c n F}{RT} \cdot (E - E_0) \right]} - e^{\left[\frac{(1 - \alpha_a) n F}{RT} \cdot (E - E_0) \right]} \right] \quad (1.19)$$

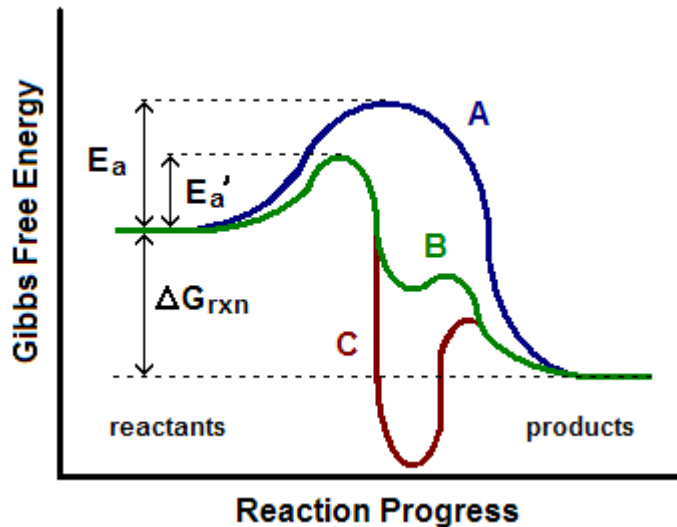


Figure 1.4: The progress of a reaction with respect to free energy for A, an un-catalyzed reaction; B, a catalyzed reaction; and C, an unproductive complex.

$$J = J_0 \cdot e^{\left[\frac{-\alpha_c n F}{RT} \cdot (E - E_0)\right]} \quad (1.20)$$

$$J = J_0 \cdot e^{\left[\frac{(1-\alpha_a) n F}{RT} \cdot (E - E_0)\right]} \quad (1.21)$$

The Butler-Volmer model provides a means to quantitatively analyze catalytic kinetics according to J_0 and α values. The Butler-Volmer model is an analog of the Arrhenius equation where J and k are both rates, J_0 and A are both pre-exponential frequencies, and the $\alpha n F (E - E_0)$ term and the E_a value both quantify the barrier energy. The efficiency of a catalyst is improved by raising exchange current density, J_0 , or by lowering the α_a or by raising the α_c for anodic and cathodic reactions, respectively.

The charge transfer coefficient, α , describes the symmetry of the energy barrier in a reaction profile. “It is fair to regard $[\alpha]$ as the heart of electrode kinetics” [26]. The symmetry of the energy barrier is determined by the intersection of semi-classical harmonic oscillators. The transfer coefficient describes symmetry according to equation 1.22 where the ϕ and ψ refer to the angles illustrated in Figure 1.5A. The angles of Figure 1.5A represent the angles of the intersecting harmonic oscillators illustrated in the boxes of Figure 1.5B. The angles of the intersections themselves do not necessarily indicate whether transfer is to higher or lower energy oscillators as represented in Figure 1.5B. Note how the Butler-Volmer equation 1.19

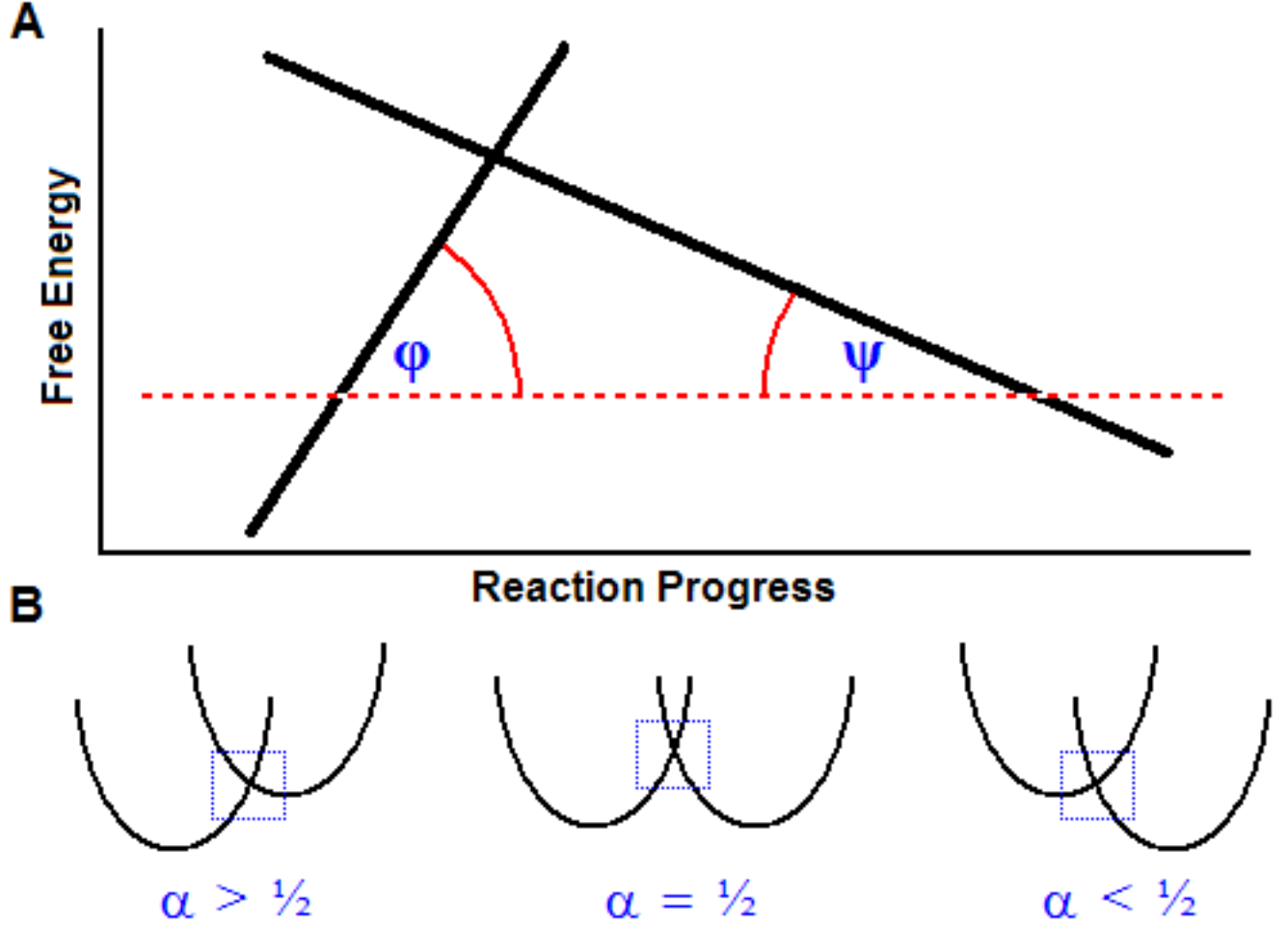


Figure 1.5: Symmetry of the charge transfer energy barriers.

treats the α coefficient differently depending on whether the reaction is cathodic or anodic. An α_c value of unity (1) represents ideal charge transfer for a reduction reaction while an α_a value of zero (0) represents ideal charge transfer for an oxidation reaction.

$$\alpha = \frac{\tan\phi}{\tan\phi + \tan\psi} \quad (1.22)$$

Quantifying catalytic kinetics requires four values to be reported. The α and J_0 values are the Butler-Volmer kinetic parameters that describe performance at low current densities. An α_a of 0 is ideal for anodic reactions, an α_c of 1 is ideal for cathodic reactions, and larger J_0 values represent better catalytic kinetics. The R_{lim} and J_b values are resistive kinetic parameters and describe how the catalytic kinetics behaves according to Ohm's law at high

current densities. Smaller R_{lim} and greater J_b values correspond to better catalytic kinetics. The R_{lim} and J_b values are determined according to equation 1.23 by performing linear regression where the kinetics are linear with respect to working potential at high current densities.

$$J = \frac{E - E_0}{R_{lim}} + J_b \quad (1.23)$$

The four kinetic values are necessary for comparing catalytic kinetics between papers. The majority of papers that will be indicated in the section concerning previous work oxygen evolution literature survey only reported an α value or a linear free energy slope (which can be converted to an α value) but did not report the J_0 or functionally equivalent value. The J_0 value had to be estimated from graphical representation to quantitatively compare kinetics. The remaining papers in the survey did not even report an α or a functionally equivalent value but only presented graphical representations of the kinetics. The majority of the papers that will be indicated in the section concerning previous work on oxygen evolution catalysis also did not report any kinetics greater than 0.10 mA/cm². The lack of information for high current densities is a problem because water electrolysis systems may operate at greater current densities in practical circumstances.

1.6 Design of Water Catalysts

The evolution of molecular oxygen from water was considered to be the less efficient of the two electrolysis reactions and the most improvement in catalytic efficiency could be accomplished here [26]. Molecular oxygen at ambient conditions is an unusual diatomic molecule in that the ground state is in the triplet state, $^1\Delta O_2$, rather than the singlet state, $^3\Sigma O_2$ [2]. A water molecule’s molecular orbital configuration must undergo a spin inversion to efficiently produce molecular oxygen in the triplet ground state. Electron spin inversions are commonly considered a forbidden reaction because spin orbit coupling creates an energy barrier for rearrangements in electron configurations [27]. We hypothesized that facilitating electron spin inversion is the key to producing molecular oxygen in the triplet state. Antibonding orbitals also create energy barriers for intermediates between water and molecular oxygen such as the superoxide ion and hydrogen peroxide states.

The energy barriers between water and molecular oxygen may be more easily appreciated in context of the oxygen reduction reaction rather than the oxygen evolution reaction.

Similar to the oxygen evolution reaction, the oxygen reduction reaction (1.1) of fuel cells is the less efficient reaction [26]. The ubiquitous presence and oxidation potential of O_2 facilitates energetically important redox reactions such as combustion and aerobic respiration. Food and fuel serve as singlet state, diamagnetic electron donors to triplet state O_2 . Thermodynamics indicate that food and fuel would spontaneously combust in the presence of O_2 but the requirement for electronic spin inversion prevents instantaneous combustion from occurring at appreciable rates unless catalyzed or ignited. The oxygen reduction reaction is several orders of magnitude slower than the hydrogen oxidation reaction in fuel cells. An approximately four-fold greater catalytic rate is required in order for state-of-the-art oxygen reduction catalysts (Pt/C platinum loaded onto carbon black) to meet automotive PEM fuel cell development targets [28]. Advances in catalyzing the oxygen evolution reaction are may promote advances in oxygen reduction catalysis.

Our development of oxygen evolution catalysts began by assessing enzymes that catalyze oxygen evolution and oxygen reduction reactions. Photosystem II efficiently produces oxygen in the triplet-state with an overvoltage of ~ 0.1 eV [29]. The overpotential for cytochrome C oxidase is less than 0.3 V [30]. The transition metal ions of the photosystem II (Mn) and cytochrome C oxidase (Fe and Cu) catalytic sites bind oxygen ligands during their catalytic cycles. The conclusions developed from studying biological reactions were that the catalytic properties of transition metal oxides ranging from Mn to Cu should be carefully explored for the oxygen evolution reaction. Co and Ni oxides were included in the exploration of Mn, Fe, and Cu oxides because they share many of the same stable aqueous oxidation states with relatively similar reduction potentials.

The scope of this work is limited to the use of first row transition metals as catalysts because these elements have the smallest electron configurations that contain d-orbitals. First row transition metals have smaller d-orbitals compared to other transition metals and therefore have smaller crystal field activation energies for transitions between oxidation states [31]. Smaller d-orbitals minimize changes in bond length during progression through a catalytic cycle. Minimizing changes in bond length during a catalytic step may result in faster kinetics by minimizing activation energies are associated with the step. Spin-orbit coupling is also small enough in d-orbitals that electron spin inversion can occur through spin crossover [27].

The first-row transition metals are more abundant than other transition metals. The first-

row transition metals are less expensive. First row transition metals ranging from vanadium to zinc are commonly found in native enzyme catalytic sites. The first-row metal ions also tend to be much more soluble in water than heavier metals.

Consideration of the whole row of transition metals allows a complete exploration of periodic trends while confining the experiments to a reasonable boundary. The periodic trend allows variation of the catalyst’s electrochemical characteristics by varying the elemental composition. Bond length, bond strength, electronegativity, and ionization energy are periodic trends that are involved with catalysis. Characterization of the first row’s trends in electrodeposition conditions and catalytic behavior will greatly facilitate the development of catalysts in future work.

A simple procedure for creating catalysts minimizes time and the number of steps and variables involved with the process. Electrodeposition is a technique in which an applied current (or voltage) drives redox chemistry so that a solid material is deposited on an electrode surface. The electrodeposition reaction enables diverse applications because catalysts can be coated onto any electrically conductive support. It was proposed that the best way to make an electrically active compound was to use an electrodeposition technique.

Nickel oxides have been formed from cathodic electrodeposition for over 100 years [32]. It has long been known that iron impurities in nickel oxides facilitate the oxygen evolution reaction, which is parasitic to the battery charging process of nickel oxide batteries [33]. Dennis A. Corrigan re-directed work originally focused on battery applications towards iron-doped nickel oxide catalysts for alkaline water electrolysis and filed a patent in 1989 [33].

The cathodic electrodeposition reaction is a simple mechanism for creating metal oxides and catalytic properties can be adjusted by exploring electrodeposition variables. The combination of natural clues from enzymes with a simple yet variable mechanism of creating catalysts was determined to be the best way to achieve ideal catalysis. The alternative route would be to computationally predict the ideal catalytic compositions. Many different strategies have been implemented for predictive catalyst design [34], [35], [36], [37], [38], [39]. Predictive catalyst design strategies based upon correlations between catalyst chemical structures, reactivity, *ab initio* calculations, and catalyst synthesis methods are still in their infancy [37]. Theoretical studies based upon first principles models using quantum chemistry are sufficiently complex to be limited by computational power even at well-defined conditions [35], [36]. The main problem associated with predictive modeling and design for

heterogeneous catalysis is attributed to a complexity far greater than traditional modeling and design applications such as pharmaceutical drug discovery methods [35], [37].

1.7 Previous Work

Catalyzing water electrolysis for the purpose of producing hydrogen for fuel has been an active area of research for over 100 years [26]. Abundant primary literature on the subject of oxygen evolution catalysis was available. The following literature survey of metal oxide catalysts only encompassed work less than ten years old except for the work of Corrigan *et al.*. Most surveyed methods of preparing the metal oxide catalysts can be categorized as hydroxide precipitation [10] [16], [40], [20], [17], [41], sol-gel methods [14], [16], [17], [18], [19], [20], [22], [42], [43], pyrolysis/thermal decomposition [15], [21], [23], [44], [45], [46], [47], [48], [49], [50] and anodic electrodeposition [12], [49], [51], [52], [53], [54], [55], [56], [57], [58], [59]. Only the catalytic work of Corrigan *et al.* in the previous decade was found to utilize cathodic electrodeposition [33], [60], [61], [62], [63], [64], [65], [66].

Careful consideration must be exercised when regarding reported catalytic kinetics. Obvious variations of reported efficiencies exist which include differences in electrolyte concentration, scale and graphical orientation, or the use of linear voltammetry scans vs Tafel plots. The temperature, atmospheric O₂ partial pressure, electrolyte concentration, and electrolyte activity values are required to calculate the oxygen evolution potential. The majority of the surveyed literature did not report how the oxygen evolution potential was calculated or what the oxygen evolution potential was considered to be. The reported current densities or potentials may have been adjusted. For example, the current density may have been adjusted to account for surface area roughness [10], [43] or for Ohmic drop compensation [45], [51], [52], [53]. Careful scrutiny revealed one report in which 956 mV was been subtracted without any justification [49].

The majority of the surveyed papers concerned alkaline water electrolysis utilizing 1 M KOH [10], [11], [12], [13], [14], [15], [16], [17], [18], [19], [20], [21], [22], [23], [63], although 1 M NaOH [44], [53] or other concentrations of KOH [18], [48] were used. The alkaline oxygen evolution catalysts were usually composed of first row transition metal oxides and specifically cite the M₃O₄ oxidation state where M was a mixture of Mn, Fe, Co, or Ni [10], [11], [14], [16], [17], [18], [22], [23], [53]. The acidic oxygen evolution catalysts are generally

less efficient than the alkaline catalysts except for those that defy the thermodynamic limits. Acidic oxygen evolution catalysts often included one or more expensive second or third row transition metal oxide such as iridium or ruthenium [40], [41], [42], [43], [45], [46], [47], [49], [50], [52], [67]. Hashimoto *et al.* reports on several anodically deposited manganese oxide-based oxygen evolution catalysts for seawater electrolysis [54], [55], [56], [57], [58], [59]. Hashimoto *et al.*'s manganese oxide catalysts catalyzed oxygen evolution over the evolution of toxic chlorine gas (Cl_2) with good selectivity and efficiency.

The best oxygen evolution catalytic kinetics of the literature survey constituted oxides containing first row metals operating in alkaline solution. Figure 1.6 illustrates the best kinetics (in terms of current density at a given potential) reconstructed from the work of Miller *et al.*, Musiani *et al.*, and Corrigan *et al.* in 1 M KOH and room temperature. The represented work Miller *et al.* was a reactively sputtered iron-doped nickel oxides with 3.2 % Fe [15]. The represented work of Musiani *et al.* reported the best alkaline efficiencies at low current densities with a PbCo oxide cathodically deposited from a sulfamic acid solution containing Pb^{2+} , Co^{2+} , and 2 % (mass/volume) C_3O_4 particles [53]. The represented work of Corrigan *et al.* was a NiFe oxide with 1 % Fe cathodically deposited from a nitric acid solution containing Ni^{2+} and Fe^{3+} at low current densities (8 mA/cm² [68]. The work of Corrigan *et al.* was the only work that utilized cathodic deposition of metal oxides, similar to the methods developed in this work. Corrigan reported the best electron transfer slopes achieving 17 mV/decade current although this catalyst produced lower current densities than the catalyst illustrated in Figure 1.6 for that current range [68]. Based upon the original graphical representations of the kinetics represented in Figure 1.6, Miller's catalyst had an α_a of 0.31 and a J_0 of -16.7 A/cm², Musiani's catalyst had an α_a of 0.75 and a J_0 of -3.9 A/cm², and Corrigan's catalyst had an α_a of 0.43 and a J_0 of -11.0 A/cm².

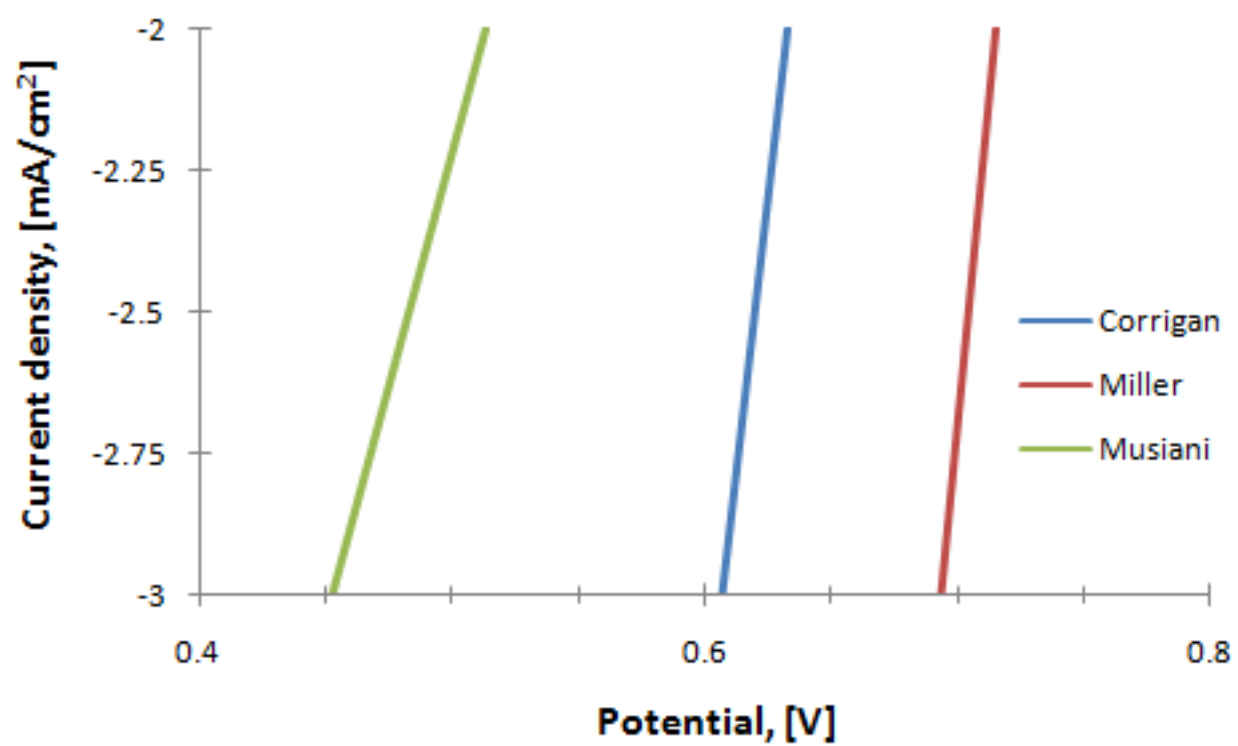


Figure 1.6: Previous work on oxygen evolution catalysts.

CHAPTER 2

CURRENT METHODS

2.1 Cell set-up

The electrochemical experiments were powered with Radiometer Analytical's Voltalab 10 (PGZ100) electrochemical workstation operated by VoltaMaster 4 software. The Voltalab 10 system has an A/D IN signal of ± 2000 mV with a 16 bit processor for a voltage resolution of $60 \mu\text{V}$. The electrochemical cell consisted of a three-electrode setup including an Accumant sat. Ag/AgCl reference electrode (13-620-53). The tip of the reference electrode was placed at the center of the catalyst/electrolyte interface of the working electrode.

The working and counter electrodes consist of square $1 \text{ cm} \times 1 \text{ cm} \times 25 \mu\text{m}$ pure platinum foil purchased from Hauser and Miller. The back of the platinum was insulated with Starbrite liquid electrical tape insulating the back of the platinum electrode so that only one flat surface area of 1 cm^2 is exposed to the electrolyte. 30 gauge platinum wires also insulated with liquid electrical tape connected the electrodes to the electrochemical workstation leads. Platinum was selected for use as both a control as well as a recyclable, electrically conductive support upon which the metal oxide catalysts were deposited. Catalyst oxides were removed with concentrated H_2SO_4 .

2.2 Electrolyte and equilibria calculations

All water electrolysis experiments were performed in ambient conditions and in atmospheric equilibrium. The laboratory temperature ranged from 22 - 24 C. Atmospheric partial pressures of 0.2095 atm O_2 and 5×10^{-5} atm H_2 were used to calculate equilibrium potentials [69]. The pH used for calculating midpoint potentials in 1 M KOH was 13.84 [9]. The equilibrium potentials for 1 M KOH were calculated to be 0.399 V for oxygen evolution according to equation 1.6 and 0.945 V for hydrogen evolution according to equation 1.12.

The equilibria calculations for the metals are provided in Appendix B. Water (Barnstead, EASYpure UV) purified to 18 Mohm resistance was used in all aspects of every experimental procedure.

2.3 Cathodic electrodeposition conditions

Catalysts were created from electrodeposition solutions containing aqueous first row transition metal salts with one or more additional electrolytes and adjusted pH. The catalysts were deposited from the electrodeposition solution compositions reported in Table 2.1 and deposited at 250 mA/cm² for 30 s unless otherwise noted. The aqueous transition metal ions were cathodically deposited as metal oxides onto the working electrode with chronopotentiometry at high current densities. The electrodes and catalyst were rinsed with purified water immediately following electrodeposition. The catalysts underwent two or more identical 1 mV/s linear voltammetry scans in 100 ml samples of 1 M KOH to discharge the catalysts and assess the catalytic kinetics.

2.4 Linear voltammetry scan

A linear voltammetry scan changes the applied working potential at a constant rate. Linear voltammetry scans were utilized in this work to measure catalytic kinetics. Linear voltammetry scans were measured from 0.380 to 0.600 V for oxygen evolution catalysts and from -0.800 to 1.300 V for hydrogen evolution catalysts in 1 M KOH solutions at a rate of 1 mV/s. The catalysts underwent two or more linear voltammetry scans. The first scan discharged and polarized the catalyst. The second scan produced a clean and accurate relationship of current density with respect to potential by which kinetics was assessed.

The kinetics of a catalyst were described with four kinetic parameters (α , J_0 , R_{lim} , and J_b) measured from linear voltammetry scans. The R_{lim} and J_b values are the two resistive kinetic parameters of equation 1.23 and were measured with linear regression from linear voltammetry scans at high current densities where current density was linear with respect to overpotential. The α and J_0 values are the two Butler-Volmer kinetic parameters and were measured according to equations 1.20 or 1.20 for the hydrogen and oxygen evolution reactions, respectively. The α and J_0 values were measured with linear regression from Tafel plots where the log of the current density was linear with respect to overpotential. The linear

Table 2.1: Electrodeposition solution conditions.

oxide	metal salt(s)	electrolyte(s)	pH
O ₂ catalysts			
Mn	18 mM MnSO ₄	125 mM NH ₄ ClO ₄	1.5 w/ H ₂ SO ₄
Fe	18 mM FeSO ₄	100 mM NH ₄ ClO ₄	1.5 w/ H ₂ SO ₄
Co	18 mM CoSO ₄	35 mM NH ₄ ClO ₄	6.8 w/ NH ₄ OH
Ni	18 mM NiSO ₄	25 mM NH ₄ ClO ₄	6.0 w/ NH ₄ OH
Cu	10 mM CuSO ₄	30 mM NH ₄ ClO ₄	5.0 w/ NH ₄ OH
FeMn	9 mM FeSO ₄ , 9 mM MnSO ₄	87.5 mM NH ₄ ClO ₄	2.5 w/ H ₂ SO ₄
CoFe	10 mM CoSO ₄ , 9 mM FeSO ₄	30 mM NH ₄ ClO ₄	5.4 w/ NH ₄ OH
NiFe(a)	9 mM NiSO ₄ , 9 mM FeSO ₄	25 mM (NH ₄) ₂ SO ₄	2.5 w/ H ₂ SO ₄
NiFe(b)	9 mM NiSO ₄ , 9 mM FeSO ₄	25 mM (NH ₄) ₂ SO ₄	5.9 w/ NH ₄ OH
NiCo	9 mM NiSO ₄ , 9 mM CoSO ₄	25 mM NH ₄ ClO ₄	6.6 w/ NH ₄ OH
CuFe	9 mM CuSO ₄ , 9 mM FeSO ₄	50 mM NH ₄ ClO ₄	4.2 w/ H ₂ SO ₄
CuNi	9 mM CuSO ₄ , 9 mM NiSO ₄	30 mM NH ₄ ClO ₄	7 w/ NH ₄ OH
H ₂ catalysts			
V	18 mM VOSO ₄	75 mM NH ₄ ClO ₄	1.25 w/ H ₂ SO ₄
Cr	9 mM Cr ₂ (SO ₄) ₃	75 mM NH ₄ ClO ₄	1.0 w/ H ₂ SO ₄
Mn	18 mM MnSO ₄	87.5 mM NH ₄ ClO ₄	1.0 w/ H ₂ SO ₄
Co	18 mM CoSO ₄	87.5 mM NH ₄ ClO ₄	5.0 w/ H ₂ SO ₄
Ni	18 mM NiSO ₄	75 mM NH ₄ ClO ₄	3.6 w/ H ₂ SO ₄
Cu	18 mM CuSO ₄	87.5 mM NH ₄ ClO ₄	1.0 w/ H ₂ SO ₄
NiV	9 mM NiSO ₄ , 9 mM VOSO ₄	37.5 mM (NH ₄) ₂ SO ₄	2.5 w/ H ₂ SO ₄
NiCr	9 mM NiSO ₄ , 9 mM Cr(ClO ₄) ₃	100 mM NH ₄ ClO ₄	3.5 w/ H ₂ SO ₄
NiMn	9 mM KMnO ₄ , 9 mM NiSO ₄	75 mM Na ₂ CO ₃	14 KOH
NiFe	9 mM NiSO ₄ , 9 mM FeSO ₄	25 mM (NH ₄) ₂ SO ₄	2.5 w/ H ₂ SO ₄
NiCo	9 mM NiSO ₄ , 9 mM CoSO ₄	75 mM NH ₄ ClO ₄	5.7 w/ H ₂ SO ₄
NiCu	9 mM NiSO ₄ , 9 mM CuSO ₄	75 mM NH ₄ ClO ₄	4.9 w/ H ₂ SO ₄
CuCo	9 mM CuSO ₄ , 9 mM CoSO ₄	75 mM NH ₄ ClO ₄	3.0 w/ H ₂ SO ₄

regression lines were measured for regions where the R² value was greater than 0.95.

2.5 Cyclic voltammetry

Cyclic voltammetry scans the applied working potential back and forth between two defined potentials at a defined potential velocity. Three cycles were measured for potential velocities ranging from 1 to 200 mV/s on the NiFe oxide from 0.200 to -0.200 V to assess

oscillation signals and from -0.700 to -1.000 V to assess capacitance and morphology. The average current densities measured from -0.985 to -1.000 V were used to determine capacitance. The values of C_d , $C_{d,e}$, $C_{d,i}$, and φ were otherwise determined according to the technique of Da Silva *et al.* [25].

2.6 Chrono coulometry

A chrono coulometry scan applies a constant potential and measures the resulting current through time. Chrono coulometry scans were used in this work to establish a steady state at a given potential preceding an electrochemical impedance spectroscopy scan at that potential.

2.7 Chrono potentiometry

A chrono potentiometry scan applies a constant current and measures the resulting potential through time. Chrono potentiometry scans were used in this work for electrodeposition reactions in which metal oxide catalysts were synthesized. Chrono potentiometry scan were also used for analyzing the durability of a catalyst by measuring how working potential changed with time at a constant current.

2.8 Electrochemical impedance spectroscopy techniques

Potential electrochemical impedance spectroscopy is a technique where a voltage sine wave is imposed upon the working potential. The experimenter defines the average working potential, the voltage sine wave amplitude, the frequency range, and the resolution in terms of data points per decade frequency. The applied voltage sine wave causes a current sine wave. A sine wave peak is the easiest point of a wave to define and measure and a vector is used to quantify the relationship of the current sine wave peak with respect to the voltage sine wave peak. The scalar is the impedance, Z , and the angle is the phase angle, θ . Impedance has the units of resistance (ohms or $\frac{V \cdot s}{C}$). The impedance vector is composed of real and imaginary values. The real resistance, Z_R , and imaginary resistance, Z_I , are derived from the impedance resistance, Z , and phase angle, θ , according to equations 2.1 - 2.3 as illustrated in Figure 2.1.

$$Z_R = Z \cdot \cos(\theta) \quad (2.1)$$

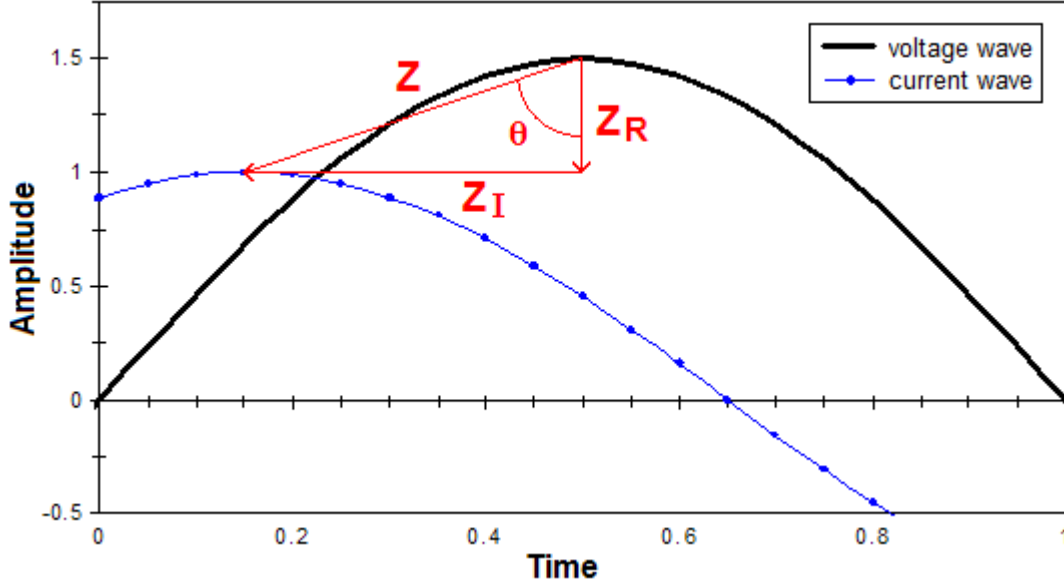


Figure 2.1: How to determine impedance, Z , real impedance, Z_R , imaginary impedance, Z_I , and phase angle, θ , from the difference in voltage and current sine waves.

$$Z_I = Z \cdot \sin(\theta) \quad (2.2)$$

$$Z^2 = Z_R^2 + Z_I^2 \quad (2.3)$$

Potential electrical impedance spectroscopy was used to model the electromagnetic behavior of the metal oxide catalysts and to elucidate catalytic mechanisms. EIS was performed in 300 mL samples 1 M KOH at room temperature and pressure. Impedance was collected at a 10 mV working potential resolution where each scan measured 20 data points per decade from 10^5 to 10^{-2} Hz with a 10 mV wave amplitude. A 2 minute chrono coulometry scan preceded each spectrum to stabilize the catalyst before measuring impedance. The electrochemical workstation responded to excessive capacitance with a safety mechanism called current disjunction at lower working potentials and frequencies.

Nyquist plots were used to illustrate the relationship of real resistance, Z_R , with respect to imaginary resistance, Z_I . The fundamental equivalent (Randel's) circuit illustrated in Figure 2.2A produces the Nyquist plot illustrated in Figure 2.2B and the values of solution resistance (R_{soln}) and charge transfer resistance, (R_{ct}) are indicated. The semi-circle of the Nyquist plot in Figure 2.2B is referred to as a capacitive loop whereas an inverted semi-circle would be referred to as an inductive loop.

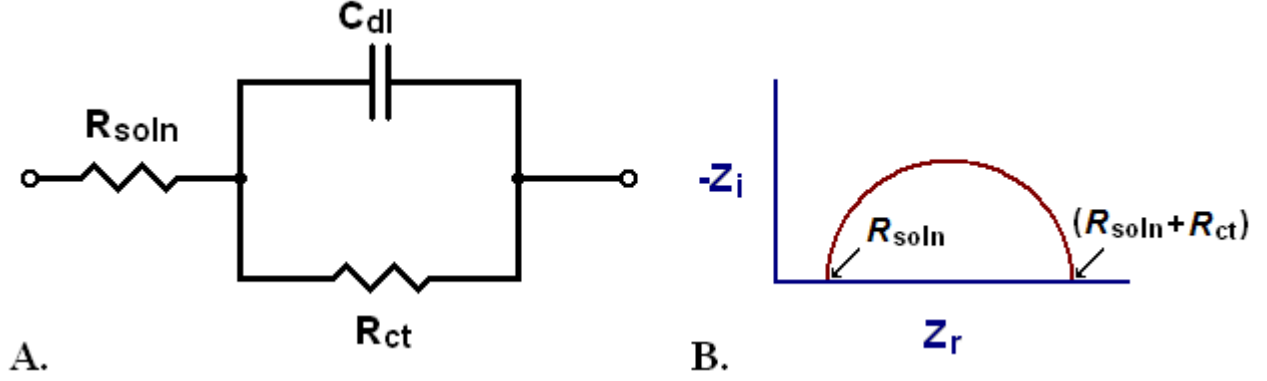


Figure 2.2: A. An equivalent circuit that produces the Nyquist plot illustrated in B where R_{soln} is the solution resistor, C_{dl} is the double layer capacitor, and R_{ct} is the charge transfer resistor. B. A Nyquist plot indicating how the values of R_{soln} and R_{ct} are measured.

2.9 Scanning electron microscopy

Elemental analysis and SEM images of the optimized NiFe oxide and the bare platinum support were obtained with a Jeol JSM-5900 Scanning Electron Microscope at 30 KeV. Elemental analysis measurements sampled five areas on the electrode surface: in the center (where the reference electrode was placed), and up, down, left, and right of the center.

2.10 Powder X-ray crystallography

Powder X-ray crystallography was performed with theta/2-theta scans at $2^\circ/\text{min}$ were performed on a Siemens D500 Diffraktometer with a Cu source. The Scherrer equation 2.4 was used to evaluate the width of metal oxide particles, where λ is the wavelength of the Cu source (0.154 nm), B is the width of the peak, and θ is the Bragg angle (1/2 the angle at which the peak is measured).

$$\text{particle width} = \frac{0.9 \cdot \lambda}{0.5B \cdot \cos(\theta)} \quad (2.4)$$

2.11 X-ray photoelectron spectroscopy

XPS binding energies were measured both before and after 5 minute sputtering with Argon ions (1 keV) at 200 nA using a vacuum Generator ESCA 2 X-ray photoelectron

spectrometer with an Al-K α source.

CHAPTER 3

Results and Discussion

3.1 Catalytic kinetics and performance

First row transition metal oxide catalysts were deposited onto platinum support electrodes. The kinetic performances of the catalysts were optimized by systematic exploration of the electrodeposition variables. The optimization procedure found that in NiFe and NiV oxide catalysts had the best kinetic performances for the oxygen and hydrogen evolution reactions, respectively. Figures 3.1 and 3.2 are Tafel plots of the oxygen and hydrogen evolution catalysts, respectively, produced from the electrodeposition conditions indicated in Table 2.1. The slopes of the Butler-Volmer kinetics indicated in Figures 3.1 and 3.2 represent greater than 99 % ideal electron transfer kinetics for oxygen evolution on a NiFe_(a) oxide catalyst and greater than 99.9 % ideal for hydrogen evolution on a NiV oxide catalyst.

3.2 Electrodeposition variables and catalyst optimization

The explored electrodeposition reaction variables affecting catalytic kinetics included: metal elemental composition; metal ion oxidation state; spectator ions; buffer composition; buffer concentration; pH; metal ion concentration; the order electrodeposition solution preparation steps; current density; and current duration. The number of variables and their apparently non-linear interactions with each other caused the exploration of the electrodeposition reaction to be exceedingly complex. Optimization of the electrodeposition variables was explored by correlating the effects of systematic adjustments of a single variable on catalytic kinetics. The exploration of electrodeposition variables was only limited by temperature, pressure, and reagent commercial availability.

Several factors of the electrodeposition solution other than kinetic performance played

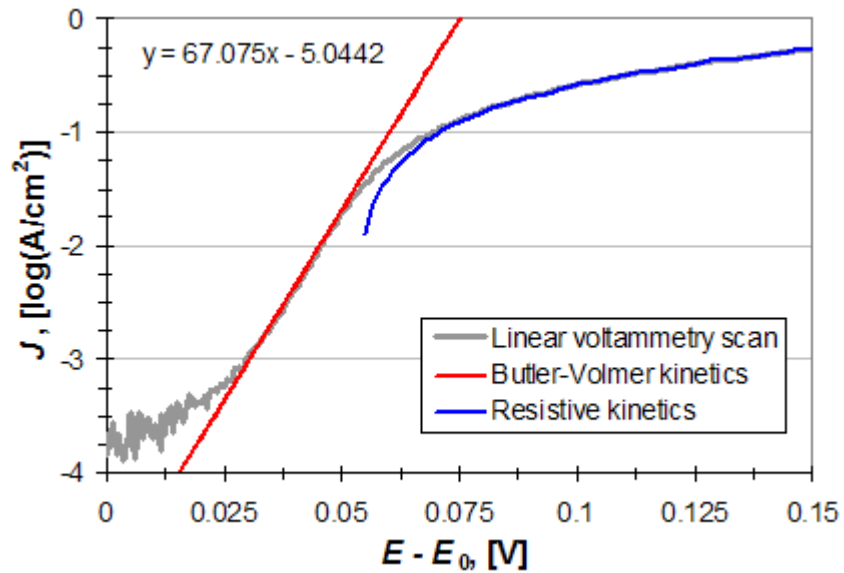


Figure 3.1: An oxygen evolution Tafel plot for a NiFe_(a) oxide catalyst. The kinetic data was collected with a linear voltammetry scan at a scan rate of 1 mV/sec in 1 M KOH, where E_0 was 0.399 V.

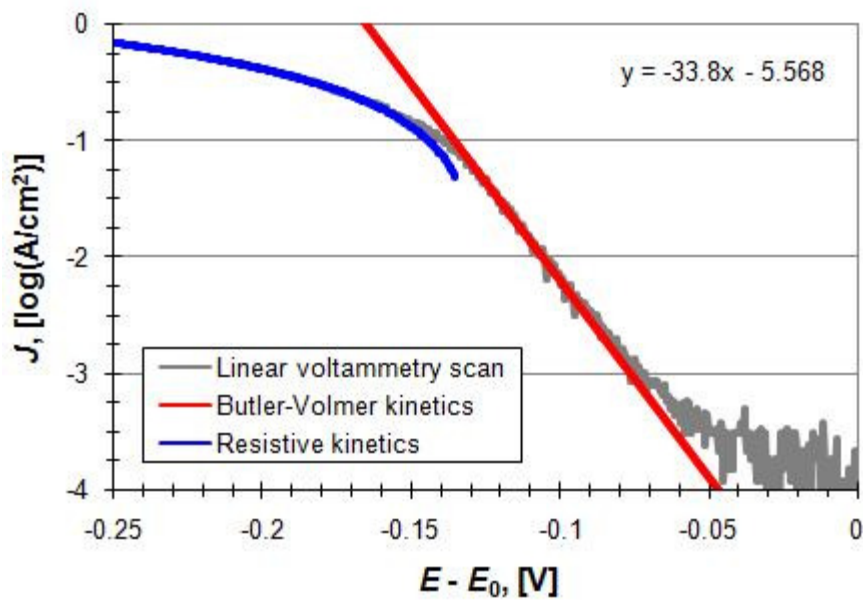


Figure 3.2: A hydrogen evolution Tafel plot for a NiV oxide catalyst. The kinetic data was collected with a linear voltammetry scan at a scan rate of -1 mV/sec in 1 M KOH, where E_0 was -0.945 V.

important roles during the exploration of variables. The electrodeposition method of creating NiFe oxide catalysts was improved so that efficiency was reproducible and the electrodeposition solutions could be made stable enough to be reused to make multiple catalysts. The electrodeposition solutions were also optimized for personal and environmental safety. For example, electrodeposition solutions containing Cl^- ions yielded competitive efficiencies but were only briefly explored because toxic Cl_2 was evolved as a byproduct during deposition.

3.2.1 The element(s) of the transition metal oxides

First-row transition metals ranging from Ti to Zn were explored. Systematic optimization of the electrodeposition variables yielded Mn, Fe, Co, Ni, Cu, FeMn, CoFe, NiFe, NiCo, CuFe, and CuNi oxides that demonstrated better alkaline oxygen evolution catalytic kinetics than the pure platinum support. The inclusion of Ti, V, Cr, or Zn into the metal oxides did not improve catalytic kinetics. The performances of four catalyst compositions were illustrated in Figure 3.3. The α_a , J_0 , R_{lim} , and J_b values of the eleven optimized metal compositions were provided in Table 3.1 so that catalytic performance could be reconstructed according to the Butler-Volmer model and equation 1.23 for each metal composition. The kinetic values reported in Table 3.1 were obtained for catalysts produced by the electrodeposition conditions reported in Table 2.1. The pure platinum foil support alone yielded a α_a of 0.155 from 0.95 – 1.00 V and a second α_a of 0.017 from 1.25 – 1.60 V.

Each metal has its own characteristic values α_a and J_0 for the oxygen evolution reaction. For example, Fe oxides tend to have better α_a values and Ni oxides tend to have better J_0 values for the oxygen evolution reaction. Better catalytic kinetics occurred when a metal with a better α_a value was combined with a metal with a better J_0 value. The ideal value for α_a is zero, so NiFe oxide's α_a of 0.0082 is greater than 99 % ideal and corresponds to a slope of 14.8 mV/decade current density. Electrodeposition conditions for NiFe oxides other than the two presented in Table 2.1 were able to achieve record values for R_{lim} (0.140 ohm) and J_0 (3.32×10^{-4} A/cm²).

Systematic optimization of the electrodeposition variables yielded V, Cr, Mn, Co, Ni, Cu, NiV, NiCr, NiMn, NiFe, NiCo, NiCu, and CuCo oxides that demonstrated better alkaline hydrogen catalytic kinetics than the pure platinum support. The NiV oxide demonstrated the best hydrogen evolution kinetics and an α_c of 0.999 (33.8 mV/decade current density). The performance of the NiV and four other catalyst compositions was illustrated in Figure 3.4.

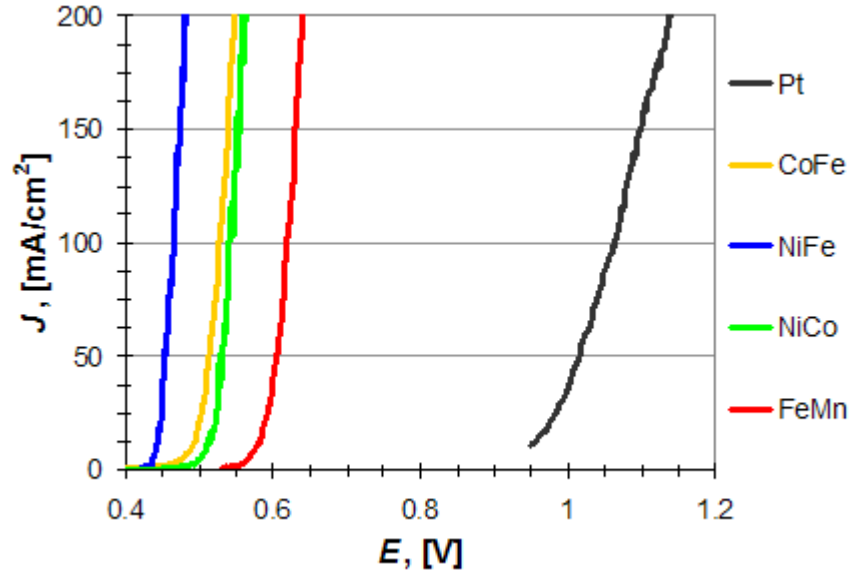


Figure 3.3: Comparison of oxygen evolution catalytic kinetics for select metal oxides against the pure platinum support collected with a linear voltammetry scan at a scan rate of 1 mV/sec in 1 M KOH.

Table 3.1: Buttlar-Volmer and Resistive kinetic parameters for oxygen evolution.

oxide	α_a	J_0 , [A/cm ²]	R_{lim} , [Ohm·cm ²]	J_b , [A/cm ²]
Mn	0.841	4.05×10^{-5}	0.181	-0.328
Fe	0.305	9.66×10^{-11}	0.209	-0.163
Co	0.660	1.39×10^{-5}	0.209	-0.158
Ni	0.694	3.73×10^{-5}	0.183	-0.149
Cu	0.795	1.12×10^{-6}	0.581	-0.309
FeMn	0.591	1.19×10^{-7}	0.187	-0.205
CoFe	0.546	1.16×10^{-5}	0.149	-0.130
NiFe	0.008	9.04×10^{-6}	0.183	-0.053
NiCo	0.515	2.17×10^{-6}	0.137	-0.140
CuFe	0.535	3.31×10^{-9}	0.168	-0.225
CuNi	0.778	1.01×10^{-5}	0.190	-0.194

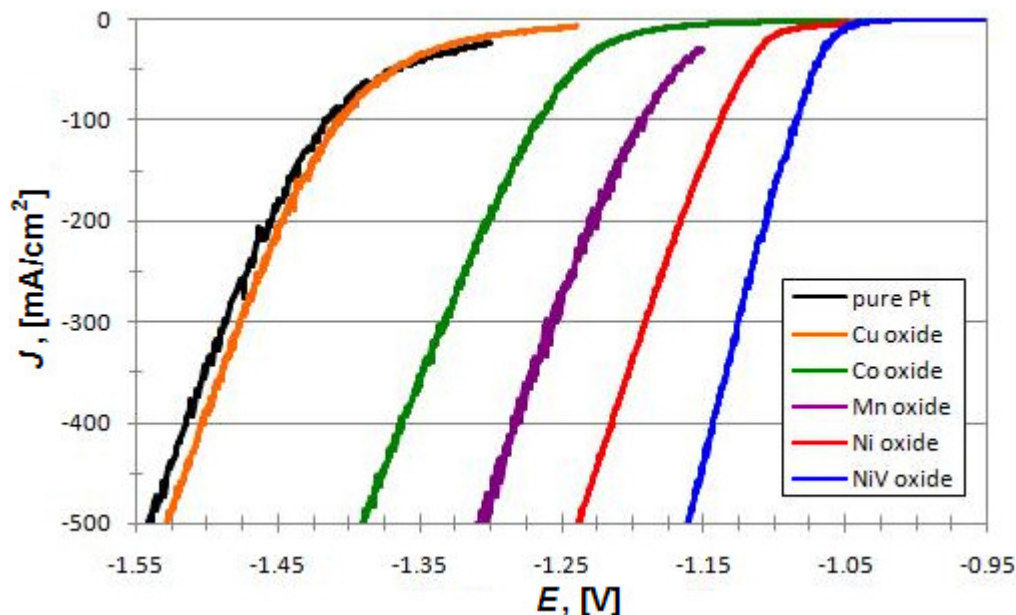


Figure 3.4: Comparison of hydrogen evolution catalytic kinetics for select metal oxides against the pure platinum support collected with a linear voltammetry scan at a scan rate of -1 mV/sec in 1 M KOH.

The α_a , J_0 , R_{lim} , and J_b values of the eleven optimized metal compositions were provided in Table 3.2 so that catalytic performance could be reconstructed according to the Butler-Volmer model and equation 1.23 for each metal composition. The kinetic values reported in Table 3.2 were obtained for catalysts produced by the electrodeposition conditions reported in Table 2.1. The pure platinum foil support alone yielded a α_c of 0.182 from -0.95 – -1.00 V.

3.2.2 The oxidation state of the aqueous metal ions in the electrodeposition solution

The oxidation states analyzed in this work was limited by the stability of the metal ion in the electrodeposition solution and by commercial availability. The stabilities of some aqueous ions, such as Fe^{2+} , required consideration. Aqueous Fe^{2+} oxidized with atmospheric O_2 and the use of stock iron solutions inhibited reproducibility. The electrodeposition conditions of $\text{NiFe}_{(a)}$ produced catalysts with kinetics comparable to $\text{NiFe}_{(b)}$, producing over 800 mA/cm^2 at 0.600 V. The pH of 5.9 of $\text{NiFe}_{(b)}$ borders the electrochemical domain of Fe^{2+}

Table 3.2: Buttlar-Volmer and Resistive kinetic parameters for hydrogen evolution.

oxide	α_c	J_0 , [A/cm ²]	R_{lim} , [Ohm·cm ²]	J_b , [A/cm ²]
V	0.543	2.25 x 10 ⁻⁵	0.302	0.708
Cr	0.535	1.50 x 10 ⁻⁵	0.325	1.008
Mn	0.418	4.99 x 10 ⁻⁴	0.250	0.948
Co	0.302	4.20 x 10 ⁻⁵	0.286	1.057
Ni	0.413	1.37 x 10 ⁻⁴	0.236	0.740
Cu	0.204	5.89 x 10 ⁻⁵	0.259	1.754
NiV	0.999	2.70 x 10 ⁻⁶	0.180	0.699
NiCr	0.844	1.37 x 10 ⁻⁶	0.212	0.926
NiMn	0.907	3.00 x 10 ⁻⁶	0.304	0.572
NiFe	0.987	6.85 x 10 ⁻⁷	0.304	0.508
NiCo	0.387	7.89 x 10 ⁻⁵	0.189	1.096
NiCu	0.397	3.53 x 10 ⁻⁴	0.188	0.997
CuCo	0.480	1.17 x 10 ⁻⁷	0.197	1.826

stability and the iron sulfate salts needed to be dissolved immediately prior to deposition to increase reproducibility. The acidic conditions of NiFe_(a) were developed later and were stable and reproducible. Pourbaix diagrams should be consulted because metal ion oxidation state stability was restricted to certain ranges of pH.

The inclusion of Fe²⁺ vs. Fe³⁺ in the electrodeposition solution provided an interesting and well-studied example of how the metal ion oxidation state affected catalytic kinetics of NiFe oxides produced from the solution. Figure 3.5 illustrates the catalytic kinetics of the electrodeposition conditions of Table 3.3 where the catalysts were all deposited at 250 mA/cm² for 30 s. Catalytic kinetics were different when Fe³⁺ was substituted for Fe²⁺ when all other variables were the same (Figure 3.5). Nearly identical efficiency could be demonstrated when most of the other variables were substantially altered.

3.2.3 The electrodeposition solution electrolyte

The electrolyte buffers the pH, facilitates higher electrodeposition current densities by increasing the ionic conductivity of the electrodeposition solution, and may have ligated or complexed the aqueous metal ions. A specroelectrochemical series of over 20 different electrolytes was explored. The majority of experiments focused on ammonium salts including

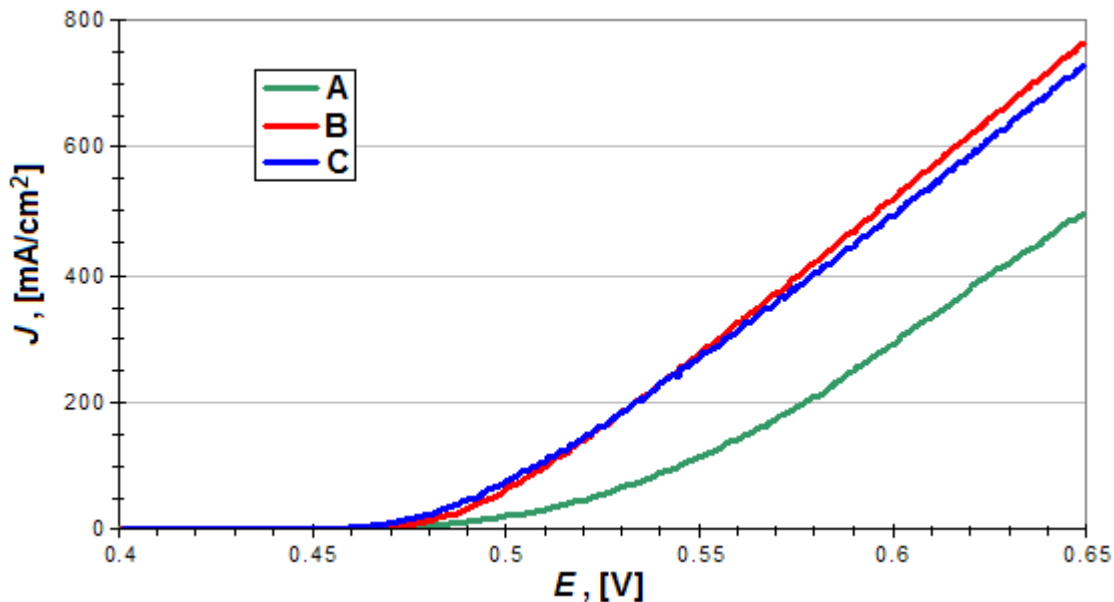


Figure 3.5: The effect of Fe^{2+} vs. Fe^{3+} in the electrodeposition conditions of Table 3.3 on catalytic kinetics of NiFe oxides.

Table 3.3: Fe^{2+} vs Fe^{3+} electrodeposition conditions for Figure 3.5.

line	Fe	Ni	electrolyte	pH
A	5.15 mM $\text{Fe}(\text{ClO}_4)_2$	12.85 mM $\text{Ni}(\text{ClO}_4)_2$	100 mM NH_4ClO_4	pH 1.8
B	5.15 mM $\text{Fe}(\text{ClO}_4)_3$	12.85 mM $\text{Ni}(\text{ClO}_4)_2$	100 mM NH_4ClO_4	pH 1.8
C	9 mM $\text{Fe}(\text{ClO}_4)_2$	9 mM $\text{Ni}(\text{ClO}_4)_2$	75 mM NH_4ClO_4	pH 5.2

sulfate, sulfite, thiosulfate, persulfate, sulfamate, hydroxide, chloride, perchlorate, monobasic phosphate, dibasic phosphate, carbonate, bicarbonate, nitrate, and acetate. The best catalytic kinetics were obtained by including ammonium sulfate, ammonium nitrate, or ammonium perchlorate electrolytes. Experimentation with organic electrolytes included acetic acid, ethanol, methanol, citrate, acetyl acetate, and ethylenediamine. The inclusion of alkali or alkaline earth metals in the electrodeposition solution consistently resulted in less efficient catalysts or no deposition at all. The effect of the electrolyte cation on catalytic kinetics is illustrated in Figure 3.6 with ammonium acetate, sodium acetate, and acetic acid in the electrodeposition solution containing 27 mM NiSO_4 and 9 mM FeSO_4 with pH

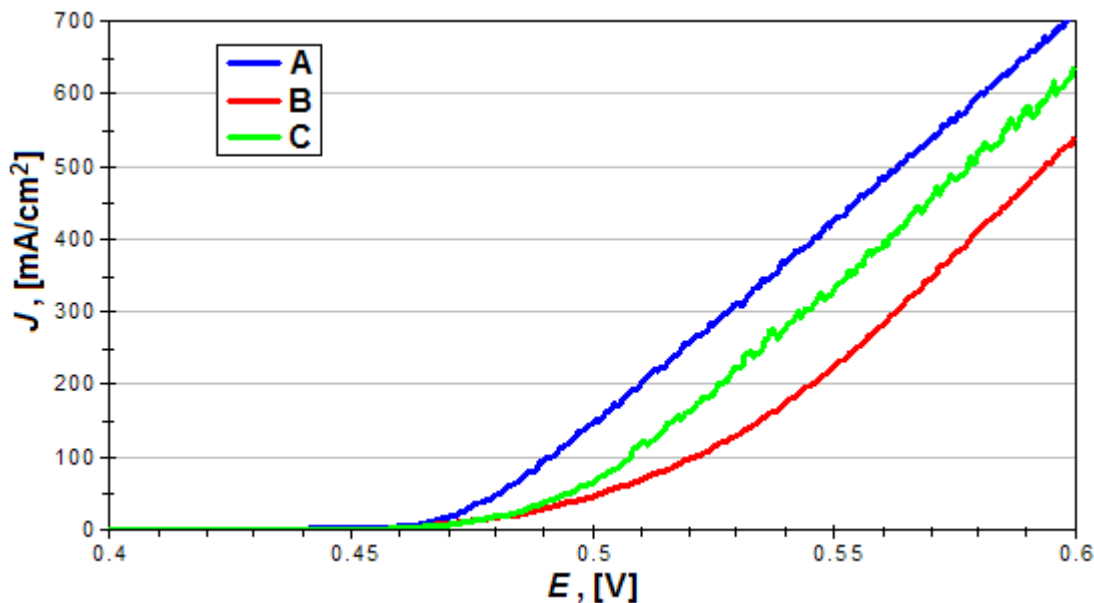


Figure 3.6: The effects of NH_4^+ , Na^+ , and H^+ in the electrodeposition electrolytes upon catalytic kinetics.

adjusted to 3.2 with H_2SO_4 and deposited at 250 mA/cm^2 for 30 s. The electrodeposition solutions also included A = 50 mM $\text{NH}_4\text{C}_2\text{H}_3\text{O}_2$, B = 50 mM $\text{NaC}_2\text{H}_3\text{O}_2$, and C = 50 mM $\text{HC}_2\text{H}_3\text{O}_2$.

3.2.4 Electrodeposition spectator ions

The effects of the metal salt's and ammonium salt's spectator ion compositions were often connected to other variables such as the metal ion oxidation state and pH. The hardness of the spectator ion affected the pH. The hardest spectator ions behaved similarly in the majority of conditions. Changes in catalytic kinetics were often correlated with the $\text{p}K_a$'s of spectator ions. The list of commercially available metal spectator anions explored included SO_4^{2-} , NO_3^- , PO_4^{3-} , Cl^- , ClO_4^- , and CH_3CO_2^- . The list of spectator cations to metal anions included Na^+ , K^+ , and NH_4^+ .

Figure 3.7 illustrates how similar catalytic kinetics resulted when the inorganic anions all had only one negative charge due to pH, were at least 1.0 pH units away from a spectator ion's $\text{p}K_a$, contained only Fe^{2+} ions, and had the same ammonium concentration. The NiFe oxide catalysts were deposited from the electrodeposition conditions of Table 3.4 and were

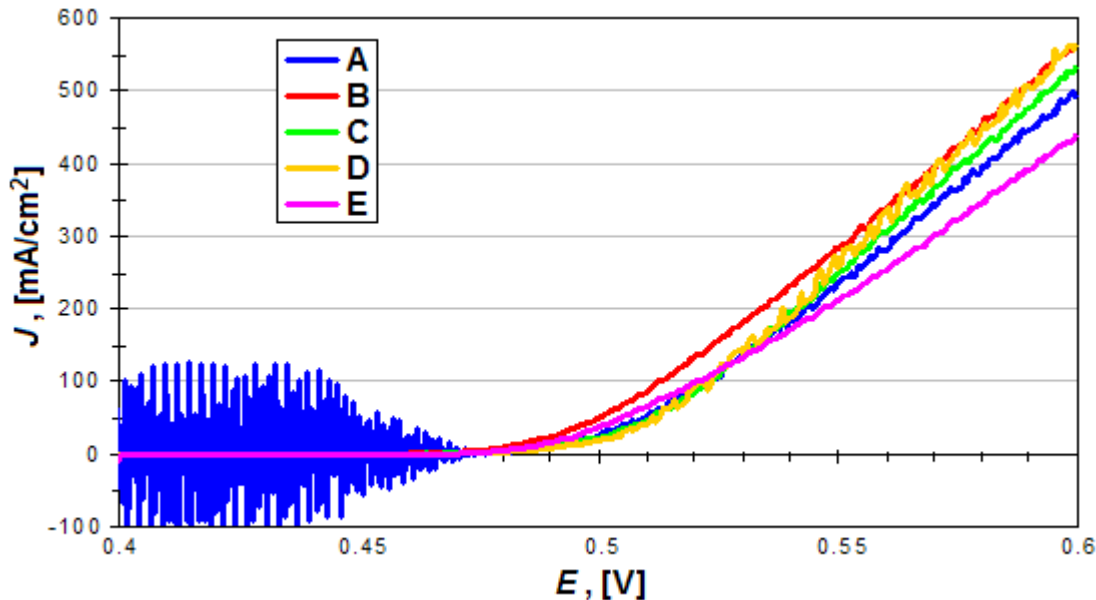


Figure 3.7: Different inorganic electrolytes had similar effects on catalytic kinetics.

Table 3.4: Spectator ion electrodeposition conditions for Figure 3.7.

line	Fe	Ni	electrolyte	pH
A	9 mM FeCl ₂	9 mM NiCl ₂	50 mM NH ₄ Cl	pH 3.0 w/ HCl
B	9 mM FeSO ₄	9 mM NiSO ₄	25 mM (NH ₄) ₂ SO ₄	pH 3.0 w/ H ₂ O ₄
C	9 mM Fe(ClO ₄) ₂	9 mM Ni(NO ₃) ₂	50 mM NH ₄ NO ₃	pH 3.0 w/ HNO ₃
D	9 mM Fe(ClO ₄) ₂	9 mM Ni(ClO ₄) ₂	50 mM NH ₄ ClO ₄	pH 3.0 w/ HNO ₃
E	9 mM FeSO ₄	4.5 mM Ni ₃ (PO ₄) ₂	50 mM H ₂ NH ₄ PO ₄	pH 3.0 w/ H ₃ PO ₄

deposited at 250 mA/cm² for 30 s.

3.2.5 The electrodeposition solution pH

The effects of the electrodeposition solution's pH were complex. All of the variables previously reviewed affected pH and were affected by pH. Reduction potentials and stabilities of the metal ions were dependent upon pH. The pH affected the interaction of the aqueous metal ions with the electrolyte whether through protonation/deprotonation of the electrolyte or by changing the strength of competing ligands. These effects were often correlated with

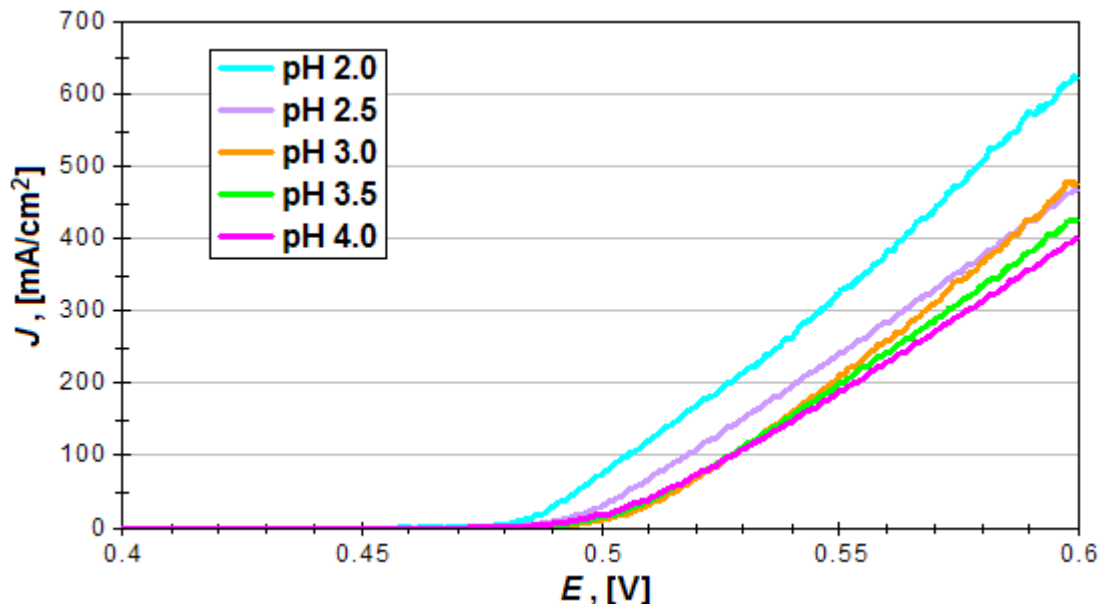


Figure 3.8: The protonation of the spectator ions ($\text{HSO}_4^-/\text{SO}_4^{2-}$) affected catalytic kinetics.

the protonation reactions of Pourbaix diagrams. The pH also affected the electrodeposition power density by changing reduction potentials and solution conductivity. Sometimes a change in 1 pH unit had negligible impact on catalytic kinetics while sometimes a change in 0.2 pH unit had significant impact at other conditions. Figure 3.8 illustrates how pH affected catalytic kinetics with respect to the pK_a of the spectator ions ($\text{pK}_a = 1.91$ for $\text{HSO}_4^-/\text{SO}_4^{2-}$) when sulfates were the only anions in the electrodeposition solution. The pH was the only variable where all five electrodeposition solutions contained 9 mM NiSO_4 and 9 mM FeSO_4 with pH adjusted with H_2SO_4 (no extra electrolytes) and deposited at 250 mA/cm² for 30 s.

3.2.6 The order of preparation steps

The order of steps by which the electrodeposition solution was prepared could affect catalytic kinetics as illustrated by Figure 3.9. All four electrodeposition solutions contained 12 mM NiSO_4 , 6 mM FeSO_4 , 30 mM $(\text{NH}_4)_2\text{SO}_4$ and 50 mM EtOH, with pH adjusted to pH 2.5 with H_2SO_4 and deposited with 250 mA/cm² for 30 s. The order of the electrodeposition solution reagents are indicated in Table 3.5. The possible dependence of catalytic kinetics on the order of electrodeposition solution preparation steps increased the number of variables

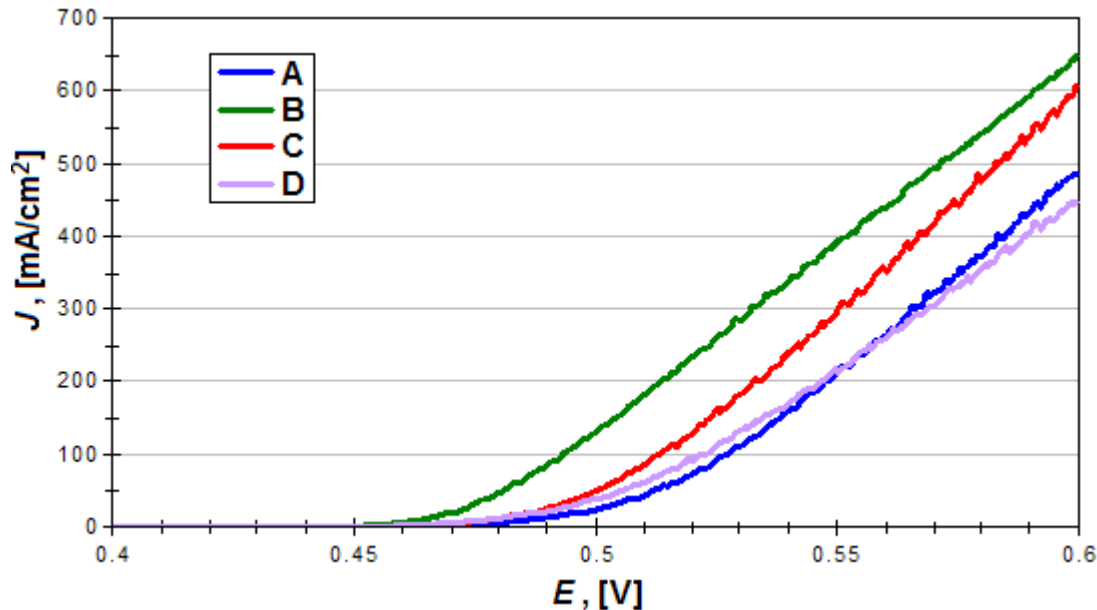


Figure 3.9: The order of electrodeposition solution preparation steps of Table 3.5 affected catalytic kinetics.

Table 3.5: The order of electrodeposition solution preparation steps for Figure 3.9.

A	nickel	ammonia	acid	iron	ethanol
B	acid	nickel	ammonia	iron	ethanol
C	acid	ethanol	nickel	ammonia	iron
D	acid	ethanol	ammonia	nickel	iron

involved with the electrodeposition reaction. The influence of the step order upon catalytic efficiency indicated complex formation in the electrodeposition solution.

3.2.7 The electrodeposition power density

Higher electrodeposition power densities resulted in better catalytic kinetics as illustrated in Figure 3.10. The catalysts were created from a solution containing 5.15 mM $\text{Fe}(\text{ClO}_4)_2$, 12.85 mM $\text{Ni}(\text{ClO}_4)_2$, and 100 mM NH_4ClO_4 , with pH adjusted with H_2SO_4 to 0.5 and deposited for 30 s with a current density of: A = 50 mA/cm²; B = 500 mA/cm². The power densities were high enough to rapidly decompose water and some electrolytes at the

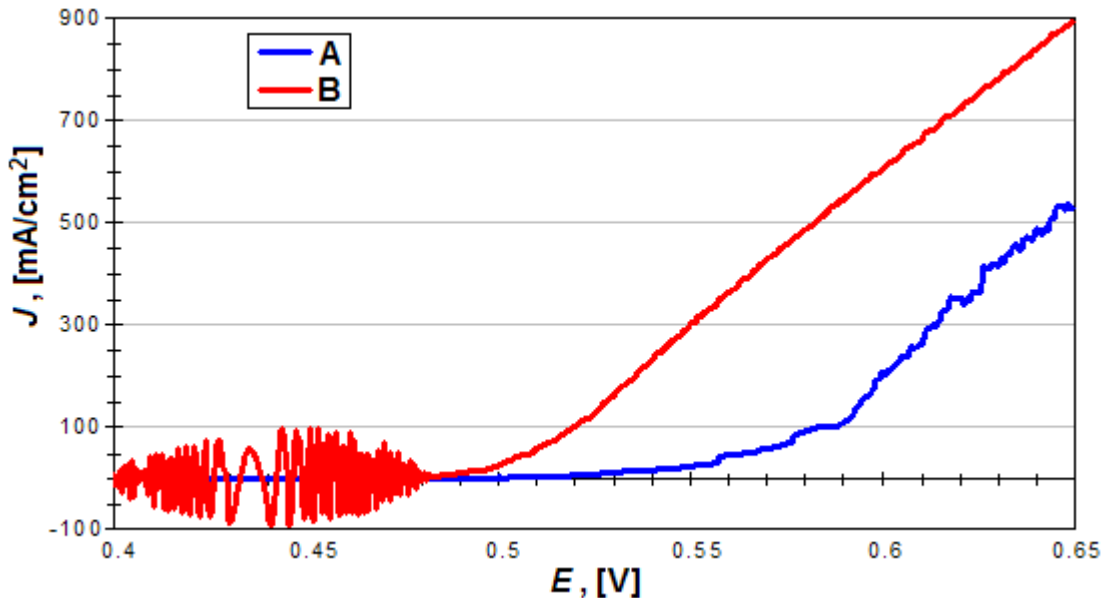


Figure 3.10: The effect of power density on catalytic kinetics.

working and counter electrodes. The following three behaviors observed for some conditions indicated that the composition of the oxides changed during deposition for some solution conditions because 1) the duration of electrodeposition affected catalytic kinetics 2) visible changes in the color and/or texture of the catalysts were observed, and 3) electrodeposition potentials changed while current was constant during electrodeposition.

3.3 Catalyst/electrolyte interaction

NiFe oxide's oxygen evolution performance was explored by varying the concentration of KOH in the electrolysis solution. Linear voltammetry scans with a velocity of 1 mV/s were collected on a NiFe oxide in 0.050, 0.100, 0.158, 0.316, 1.00, and 10.000 M KOH electrolytes. The α_a and J_0 of the NiFe oxide catalyst did not change with respect to KOH concentration. The R_{lim} remained constant above 0.316 M KOH yet became smaller at lower concentrations of KOH. Figure 3.11 illustrates the change in R_{lim} with respect to the KOH concentration by plotting the inverse of R_{lim} against the log of [KOH]. The kinetic dependence of the NiFe and other metal oxides upon KOH concentration indicated that oxygen evolution catalysis required a minimum pH of 12.7 to become partially active and became fully activated at pH

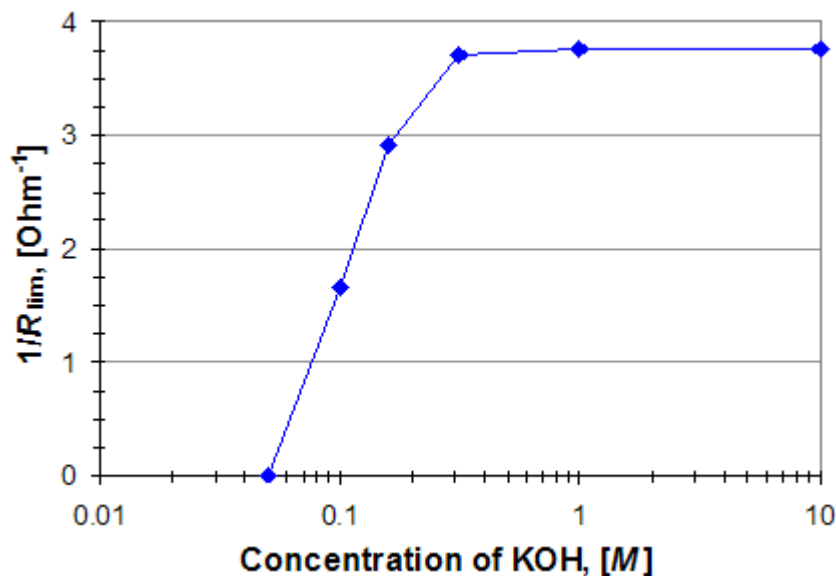


Figure 3.11: Reciprocal of R_{lim} with respect to the molar concentration of the KOH electrolyte for oxygen evolution on a NiFe oxide catalyst.

13.5.

The dependence of R_{lim} on the conductivity of the electrolyte was explored by adding KCl to the KOH solution. The presence of chloride ions did not significantly affect oxygen evolution kinetics when $[OH^-] = [Cl^-]$. The oxygen evolution reaction was inhibited when $[OH^-] < [Cl^-]$ and the evolution of Cl_2 was detected by linear voltammetry and olfaction. Other catalyst compositions demonstrated similar pH dependence and reactivity with Cl^- despite elemental composition.

Cyclic voltammetry and electrochemical impedance spectroscopy were performed on the NiFe oxide oxygen evolution catalyst to identify active half-reactions. Cyclic voltammetry scans of the metal oxide catalysts did not produce peaks that resulted from the net charge transfer of oxidation–reduction couples active within the catalyst. The metal oxide catalysts developed in this work produced oscillating signals in response to linear changes in working potential. An oscillating current in response to linear changes in working potential indicated charge movement and rearrangement within the metal oxide rather than net charge transfer between the metal oxide catalyst and the KOH electrolyte. The amplitude and frequency of the oscillation signal of Figure 2.12 could result in over a coulomb of charge rearrangement

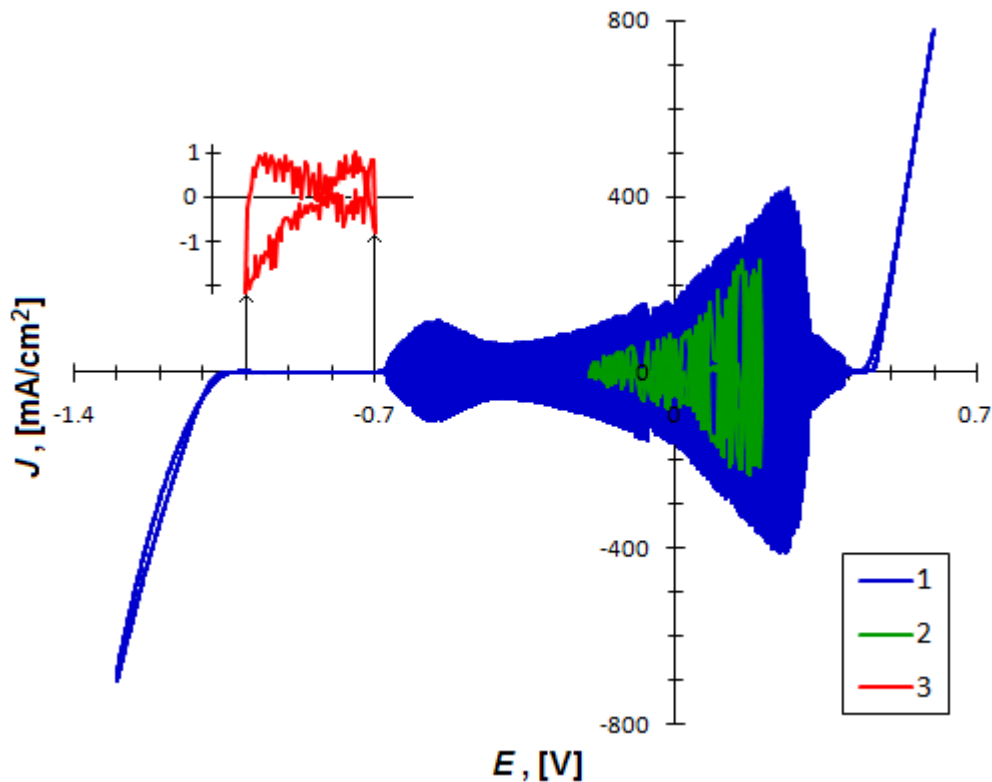


Figure 3.12: Cyclic voltammetry 1 M KOH of a $\text{NiFe}_{(a)}$ oxide catalyst at: 1) 1 mV/s between 0.600 and -1.300 V; 2) 200 mV/s between 0.200 and -0.200 V; and 3) 200 mV/s between -0.700 and -1.000 V.

within a second for slower scan rates. Analysis of the oscillations revealed that the height of the signals decreased at higher cycle velocities by 1 mA/cm² per mV/sec for the range of 1 mV/s to 200 mV/s.

The surface morphology of the NiFe oxide catalyst was electrochemically assessed with cyclic voltammetry where the catalyst demonstrated the most capacitive behavior (line 3 of Figure 3.12) according to the procedure of Da Silva *et al.* [25]. The current densities of the negative current peak were plotted against cycle velocity in Figure 3.13. The reported current densities represented the average current density of the negative peak between -0.975 and -1.000 V due to the noise of the system observed for all cycle velocities. The trend lines indicated in Figure 3.13 represent the best fit for all combinations of one or more regression lines. The NiFe oxide catalyst demonstrated two regions of linear capacitance characteristic of rugged electrode films [25]. The total differential capacitance, C_d , was measured to be

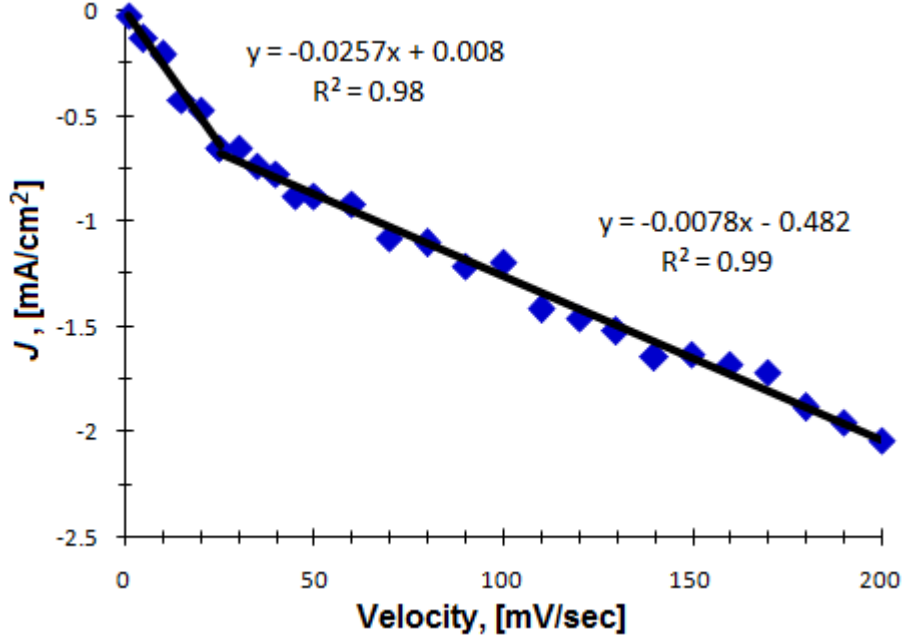


Figure 3.13: The dependence of current density, J , with respect to cyclic voltammetry velocity on a $\text{NiFe}_{(\text{a})}$ oxide in 1 M KOH.

25.7 mF, the external differential capacitance, $C_{d,e}$, was measured to be 7.8 mF, and the morphology factor, φ , was determined to be 0.70.

3.4 Impedance characterization

Chronopotentiometry scans were performed to determine short-term stability. Figure 3.14 was recorded for a NiFe oxide catalyst at 500 mA/cm² for one hour. The NiFe oxide catalysts underwent a relaxation by which the catalyst become more efficient through time. The catalysts demonstrated stability during the time scale required to collect impedance spectra and was promising for long-term durability.

EIS was performed on the NiFe oxide catalyst from 0.300 – 0.600 V in 10 mV increments so that changes in impedance with respect to working potential could be determined. Nyquist plots of 0.400 – 0.440 V and 0.450 – 0.530 V potential ranges were presented in Figures 3.15A and 3.15B, respectively. A unique feature of the Nyquist plots was the inductive loop illustrated in Figure 3.15C for 0.350 – 0.440 V. Only one arc was observed in the inductive loop below 0.390 V while two distinct arcs were observed above 0.390 V. EIS was performed

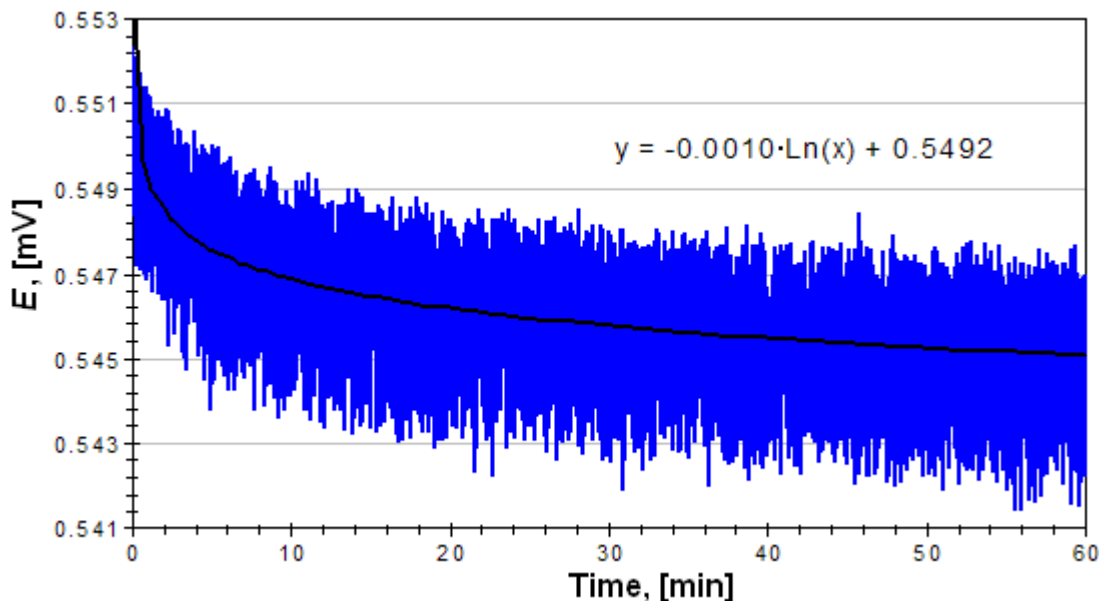


Figure 3.14: A chrono potentiometry scan on a NiFe oxide catalyzing oxygen evolution at 500 mA/cm^2 for one hour in 1 M KOH.

on the pure platinum support including the insulating backing from 0.900 – 1.500 V in 50 mV intervals. The inductive loop was not observed in the EIS spectra of the platinum without catalyst although a small amount of inductance was observed (Figure 3.15D).

3.4.1 Catalytic mechanisms

Electrochemical potentials in aqueous solutions are well known and changes in impedance spectra with respect to applied working potential were correlated with known half-reactions. Reduction potentials for the oxygen evolution reaction 1.1 and stable Ni, Co, and Fe hydrated oxidation states were calculated for pH 13.84 in 1 M KOH according to the equations reported in Pourbaix’s Atlas of Electrochemical Equilibria in Aqueous Solutions [3]. The measurement of impedance for working potentials in increments of 10 mV and with a 10 mV amplitude provided sufficient resolution for the changes in impedance spectra with respect to working potential to be correlated with known reduction potentials. Observation of the phase angle, θ , was the clearest means by which impedance spectra change with respect to working potential.

Changes in θ with respect to working potential were found to correlate with known nickel

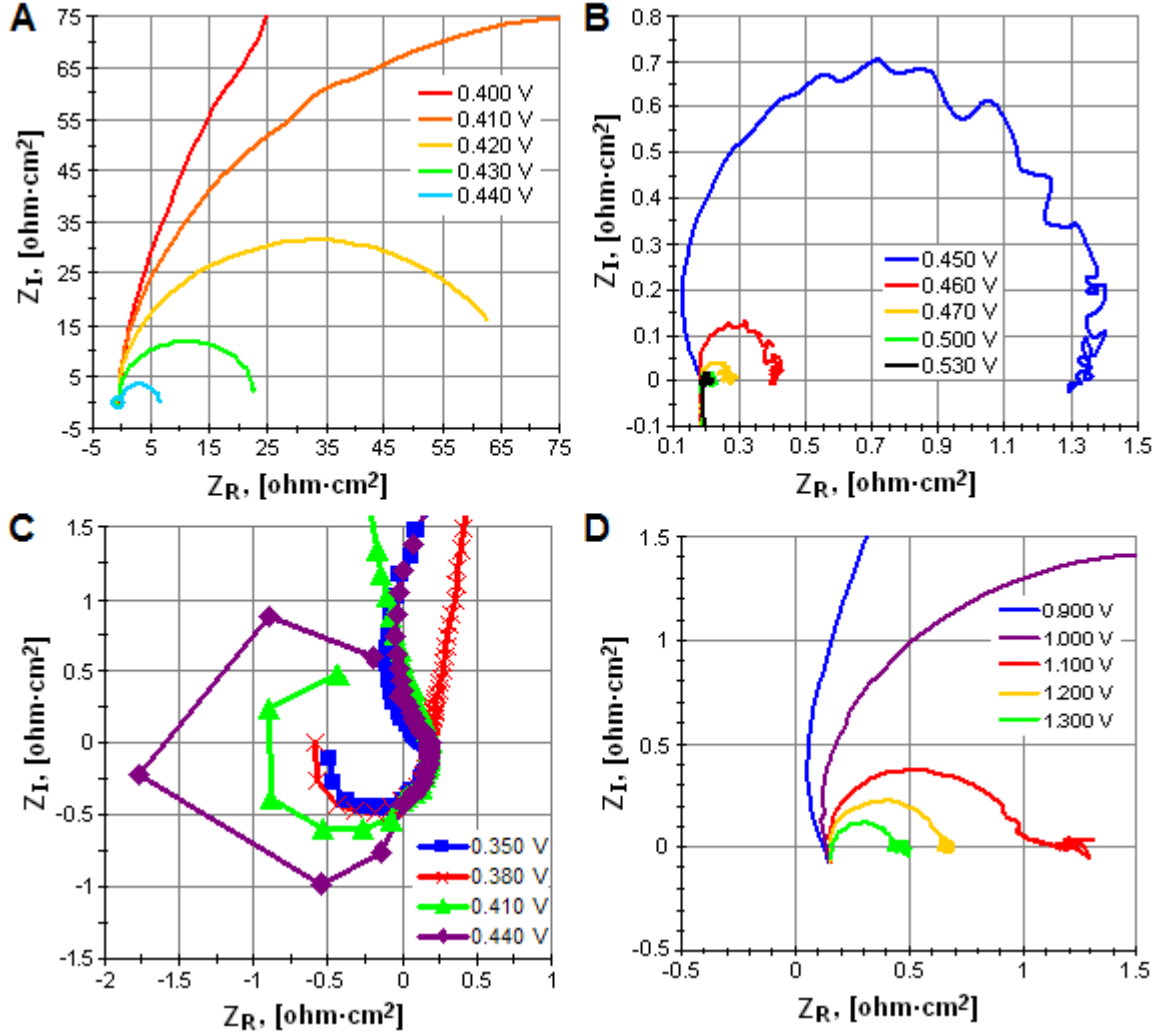


Figure 3.15: EIS Nyquist plots of a NiFe oxide electrode in 1 M KOH at (A) low working potentials, (B) at medium working potentials, and (C) the inductive loop. (D) EIS Nyquist plot of the pure platinum control in 1 M KOH.

and iron reduction potentials. The iron redox reaction of equation 3.1 correlated with both the phase angle change observed in Figure 3.16 as well as the appearance of the second arc in the high frequency inductive loop (Figure 3.15C). The combination of both reactions 3.1 and 3.2 equals 0.467 V and correlated with the phase angle's approach to zero. Reaction 3.3 was proposed as a basic catalytic mechanism for oxygen evolution by the NiFe oxide catalyst.



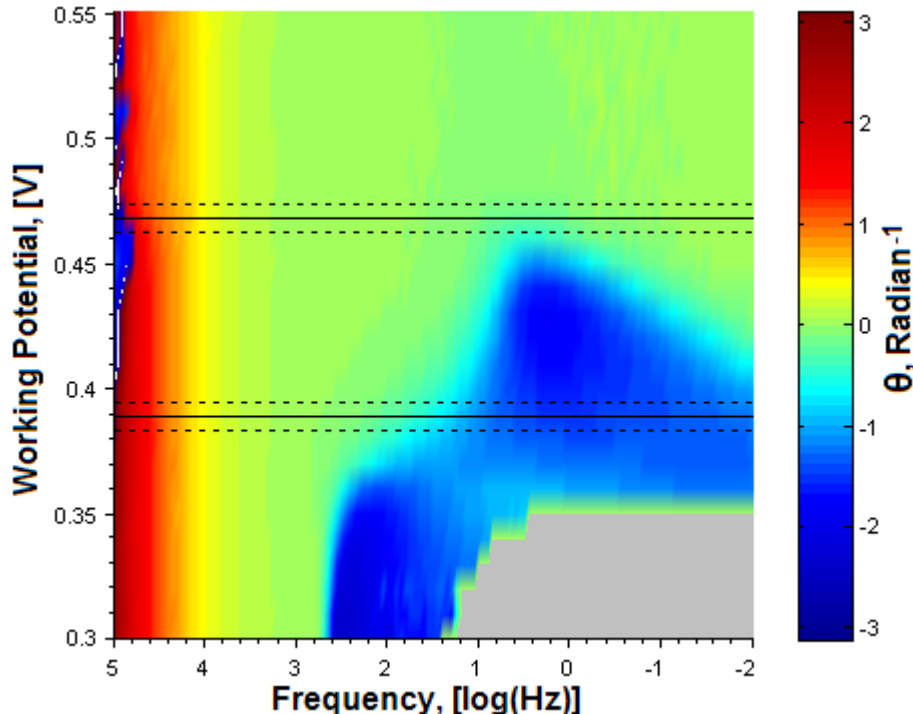
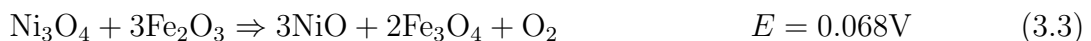


Figure 3.16: The phase angle, θ , with respect to frequency and working potential for a NiFe oxide catalyst in 1 M KOH. The solid lines indicate the electrochemical potential of nickel and/or iron half-reactions while the dashed lines mark the ± 5 mV boundary of the impedance voltage wave amplitude.



The catalysts composed of Ni, Co, and Fe, and combinations thereof demonstrated the best oxygen evolution kinetics. Ni, Co, and Fe share many of the same stable oxidation states with relatively similar reduction potentials. CoFe and NiCo oxides were examined with EIS to compare catalytic mechanisms. The correlation of CoFe and NiCo phase angles with half-reactions similar to those identified in the NiFe catalytic mechanism provided support for both the mechanism proposed above and the validity of the technique.

The phase angle of the CoFe oxide demonstrated the same behavior as the NiFe oxide (Figure 3.17). The phase angle changed in correlation with the iron reduction potential of 0.389 V for reaction 3.1. Reaction 3.4 describes a cobalt reaction equivalent to the nickel reaction observed in the NiFe mechanism. The potential combination of the iron reaction

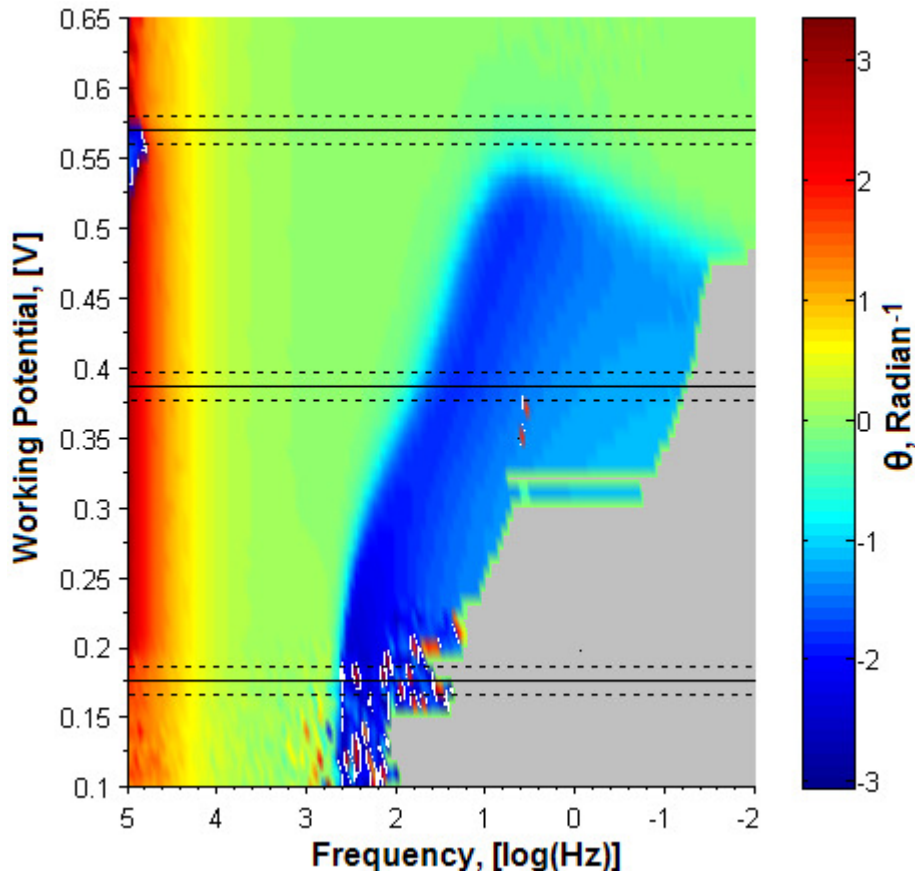
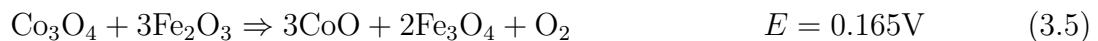
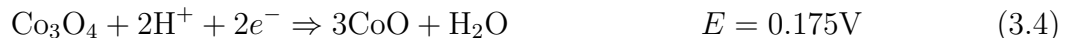


Figure 3.17: The phase angle, θ , with respect to frequency and working potential for a CoFe oxide catalyst in 1 M KOH. The solid lines indicate the electrochemical potential of cobalt and/or iron half-reactions while the dashed lines mark the ± 5 mV boundary of the impedance voltage wave amplitude.

3.1 with the cobalt reaction 3.4 equals 0.564 V and corresponded with the phase angle's approach to zero. Reaction 3.5 was proposed as the oxygen evolution catalytic mechanism for the CoFe oxide.



The phase angle of the NiCo oxide catalyst demonstrated similar yet different behavior to the NiFe and CoFe oxide catalysts (Figure 3.18). The NiCo oxides behaved similarly in that it utilized the same set of oxidation state transitions as observed for the NiFe and

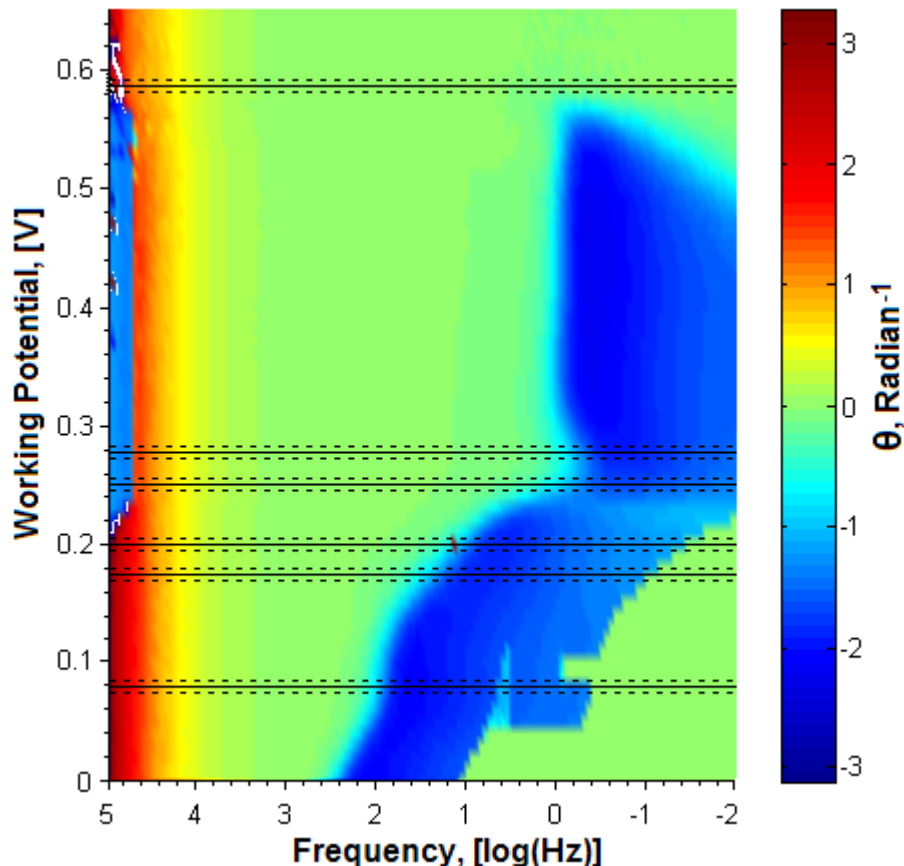


Figure 3.18: The phase angle, θ , with respect to frequency and working potential for a NiCo oxide catalyst in 1 M KOH. The solid lines indicate the electrochemical potential of nickel and/or cobalt half-reactions while the dashed lines mark the ± 5 mV boundary of the impedance voltage wave amplitude.

CoFe oxide catalysts. The NiCo oxide behaved differently in that two sets of oxidation state transitions were observed: one set in which the nickel reaction 3.2 was paired with the cobalt reaction 3.6 and one set in which the cobalt reaction 3.4 was paired with the cobalt reaction 3.6. The NiCo catalytic mechanism likely consisted of two sets of the same oxidation state transitions because the potential for each individual set (0.278 V and 0.375 V, respectively) was not great enough to drive oxygen evolution. The potential sum of reactions 3.2, 3.4, and 3.6 equals 0.588 V and correlated with the phase angle approach to zero. Reaction 3.7 was proposed for the NiCo catalytic mechanism. NiCo's phase angle changed in correlation with the three individual half-reactions and with the combinations of the half-reactions.

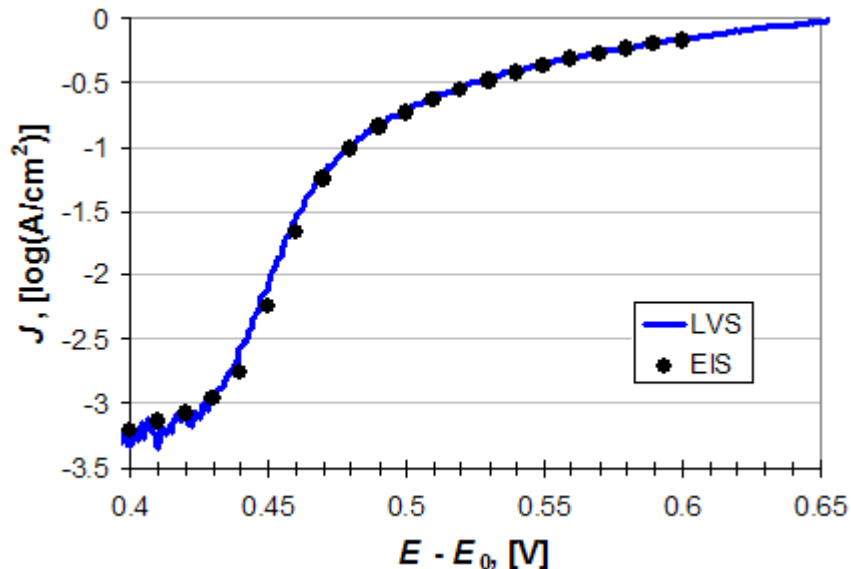
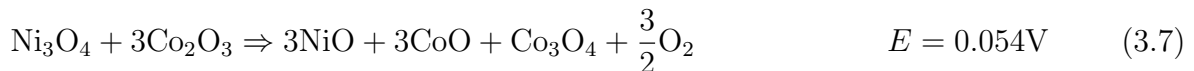


Figure 3.19: A Tafel plot of a NiFe oxide catalyst in 1 M KOH comparing the current densities measured from impedance and with a 1 mV/s linear voltammetry scan performed just prior to the impedance spectroscopy.



3.4.2 Correlating impedance with the Butler-Volmer models

A Butler-Volmer model was derived from impedance data by comparing the current densities measured during impedance with the current densities measured with a linear voltammetry scan. The current densities measured from impedance and the current densities measured with a 1 mV/s linear voltammetry scan performed just prior to the impedance spectroscopy were compared in a Tafel plot (Figure 3.19). The similarity between current densities indicated that impedance did not significantly distort current density values at low potentials or when the electrocatalyst system was non-linear.

The relationship between current density, J , and time-independent impedance, Z_R , was determined with Ohm's law 1.16. The solution resistance, R_{soln} , and charge transfer resistance, R_{ct} , are the two time-independent impedance values. It was empirically established

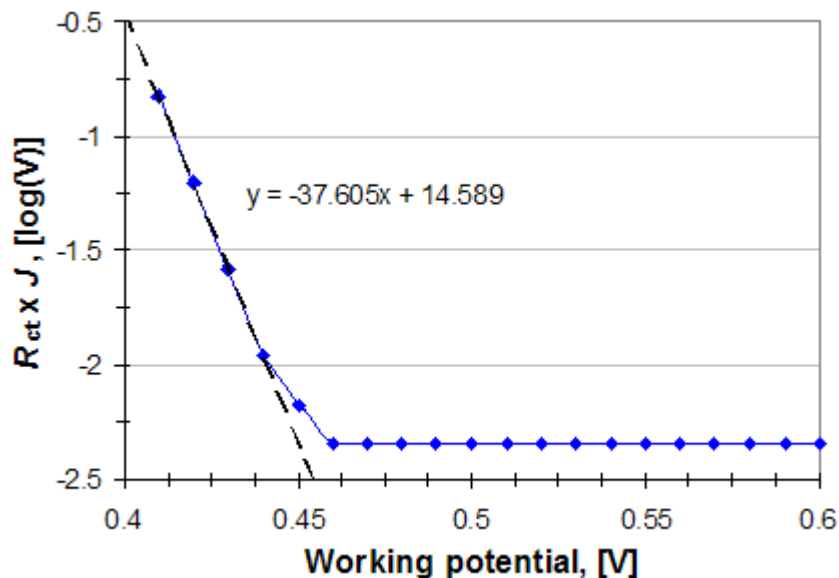


Figure 3.20: The product of R_{ct} and J with respect to working potential on a NiFe oxide catalyst in 1 M KOH.

that the R_{soln} had no effect upon current density as measured by this experimental setup because the tip of the reference electrode is in contact with the catalyst. The R_{soln} measured in this system may have been caused by the reference electrode because it did not affect the current density. It should be noted that not all R_{soln} values are necessarily experimental artifacts.

The current density was dependent upon the R_{ct} at higher working potentials for NiFe, CoFe, and NiCo oxide oxygen evolution catalysts. The product of current density and R_{ct} was 4 mV at a working potential of 0.460 V or greater for the NiFe oxide (Figure 3.20). The product of current density and R_{ct} was 4 mV at a working potential of 0.560 V or greater for the CoFe oxide (Figure 3.21). The product of current density and R_{ct} was 4 mV at a working potential of 0.600 V or greater for the NiCo oxide (Figure 3.22). A product of 4 mV for the catalysts suggested that the potential was a function of the impedance bridge circuit and/or the reference electrode rather than the catalyst composition.

The product of R_{ct} and J deviated from a constant 4 mV at lower working potentials because of the R_{ct} values and not the J values. The J values were demonstrated to conform to actual current densities in Figure 3.19. The deviation of measured R_{ct} values away from true R_{ct} values was determined by comparing anodic charge transfer coefficients, α_a . Figure 3.23

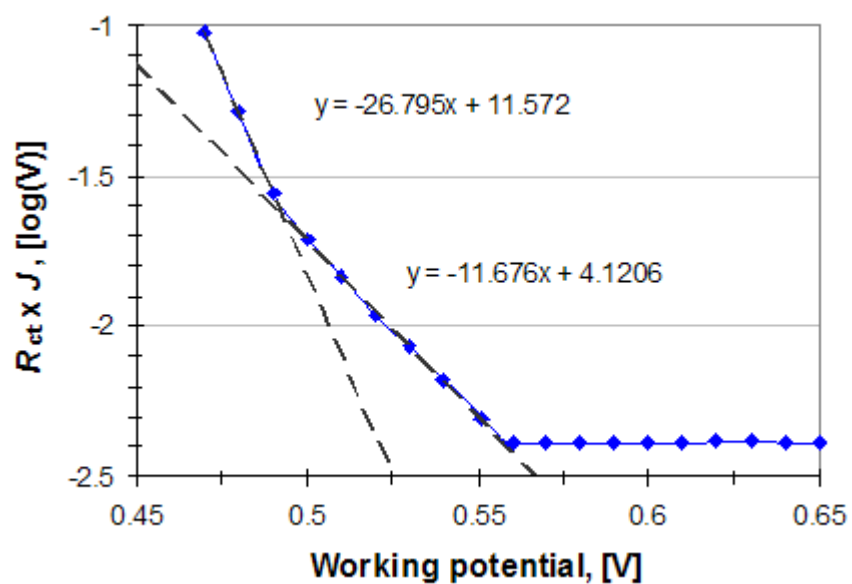


Figure 3.21: The product of R_{ct} and J with respect to working potential on a CoFe oxide catalyst in 1 M KOH.

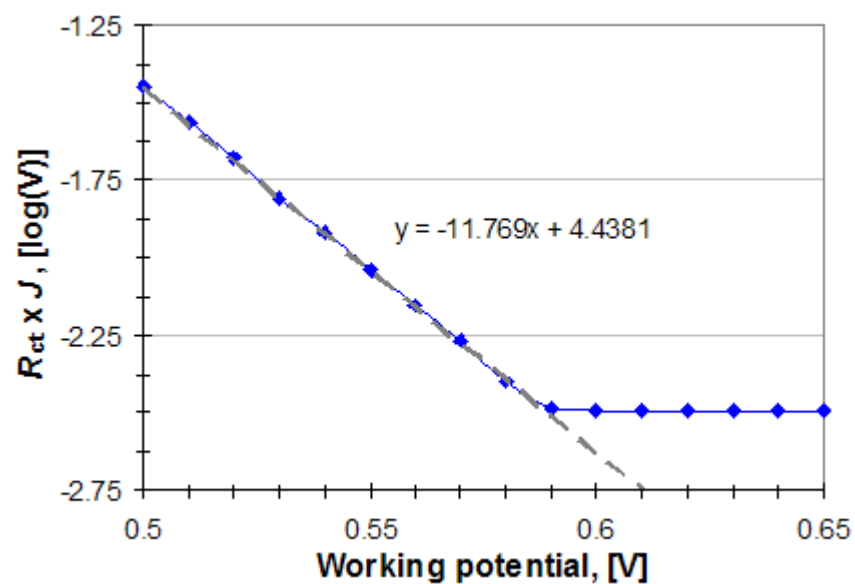


Figure 3.22: The product of R_{ct} and J with respect to working potential on a NiCo oxide catalyst in 1 M KOH.

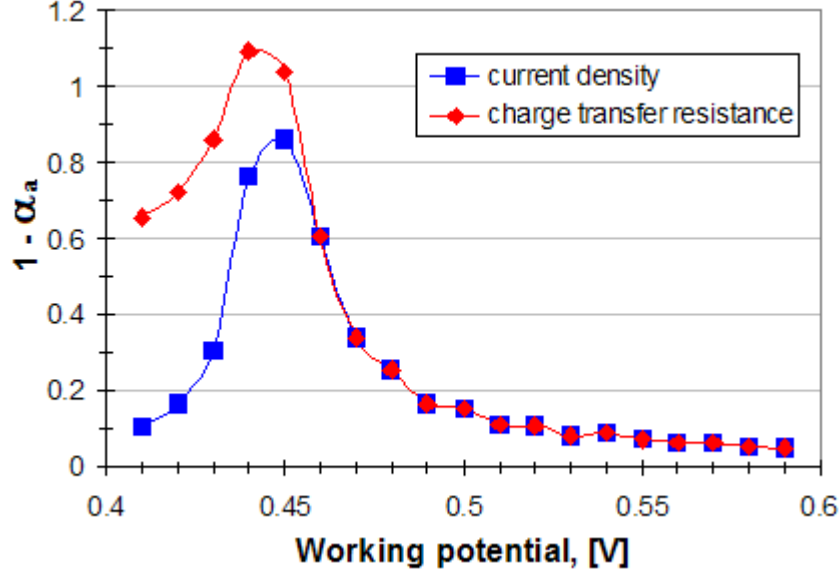


Figure 3.23: A comparison of NiFe oxide oxygen evolution charge transfer coefficients, α_a , determined by J and by R_{ct} values.

illustrates the α_a determined by J according to equation 3.8 and the α_a determined by R_{ct} according to equation 3.9. The true R_{ct} values were be kinetically determined by considering the product of J and R_{ct} to be constant at 4 mV even at lower working potentials so that the true R_{ct} values would produce the same α_a as the J values.

$$1 - \alpha_a = \frac{\Delta J R T}{\Delta V n F} \quad (3.8)$$

$$1 - \alpha_a = \frac{-\Delta R_{ct} J R T}{\Delta V n F} \quad (3.9)$$

The ratio between the true R_{ct} and measured R_{ct} values were applied to the rest of the measurements obtained for the NiFe oxide oxygen evolution spectra to remove the distortion in the impedance scalar values and obtain the true impedance values. The true Z_R and Z_I values are illustrated in Figure 3.24. The trendline indicated in Figure 3.20 was used to approximate measured R_{ct} values at the lower working potentials. Circular regression revealed that the disfiguration of the inductive loop at higher working potential was due a lack of measurement resolution rather than error in the data even though the measurements were obtained with the Voltalab 10's highest resolution (20 points per decade frequency).

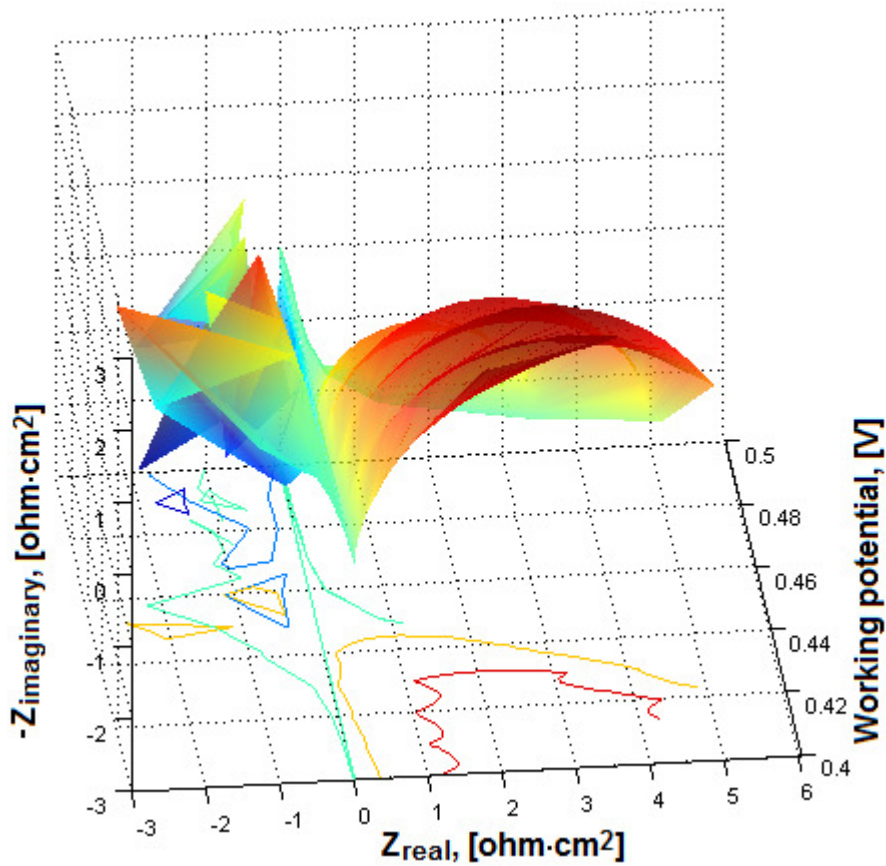


Figure 3.24: The true Z_R and Z_I values for oxygen evolution on the NiFe oxide catalyst as determined by the ratio between the true R_{ct} and measured R_{ct} values.

3.5 Catalyst chemical structure

3.5.1 Scanning electron microscopy

The NiFe_(a) and NiFe_(b) oxide oxygen evolution catalysts and the NiV oxide hydrogen evolution catalyst were analyzed with scanning electron microscopy. Images of the NiFe oxide, the NiV oxide, and the bare platinum support are presented in Figures 3.25. The catalysts were assessed with linear voltammetry scans to ensure that the catalysts had greater than 95 % ideal electron transfer coefficients. The elemental analysis averaged from five sections of the catalyst indicated that the NiFe_(a) oxide had an atomic ratio of 68.9 \pm 2.2 % Ni and 32.2 \pm 1.9 % Fe and the NiFe_(b) oxide had an atomic ratio of 72.1 \pm 0.4 % Ni and 27.8 \pm 0.5 % Fe. Potassium did not bind or become impregnated into the

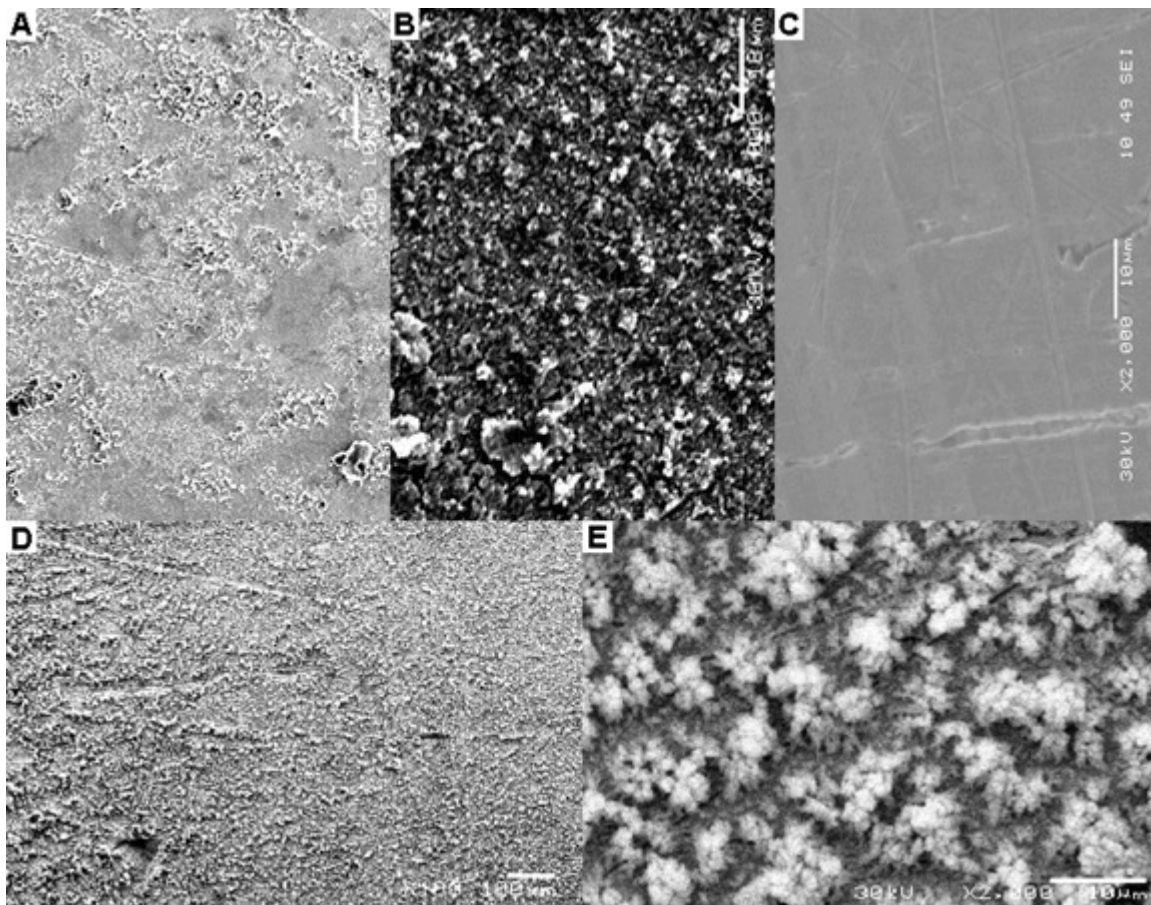


Figure 3.25: SEM images of the NiFe oxide catalyst at (A) 100X magnification and (B) 2000X magnification, the bare platinum support at (C) 2000X magnification, and the NiV oxide catalyst at (D) 100X magnification and (E) 2000X magnification.

NiFe oxide because it was only detected in one of the five sampled areas (0.17 %) after use. Silver from the Ag/AgCl reference electrode could be detected (2.5 % Ag) on the catalyst after impedance experiments where the reference electrode had been placed. Silver was not detected in three of the five other sample areas. Elemental analysis indicated that the NiV oxide had an atomic ratio of 99.2 ± 0.3 % Ni and 0.8 ± 0.3 % V. Elemental analysis also verified that the purity of the platinum from Hauser and Miller was greater than 99.95 % Pt with 0.03 % Al even after hundreds of catalysts had been deposited and stripped with concentrated H_2SO_4 from the platinum support.

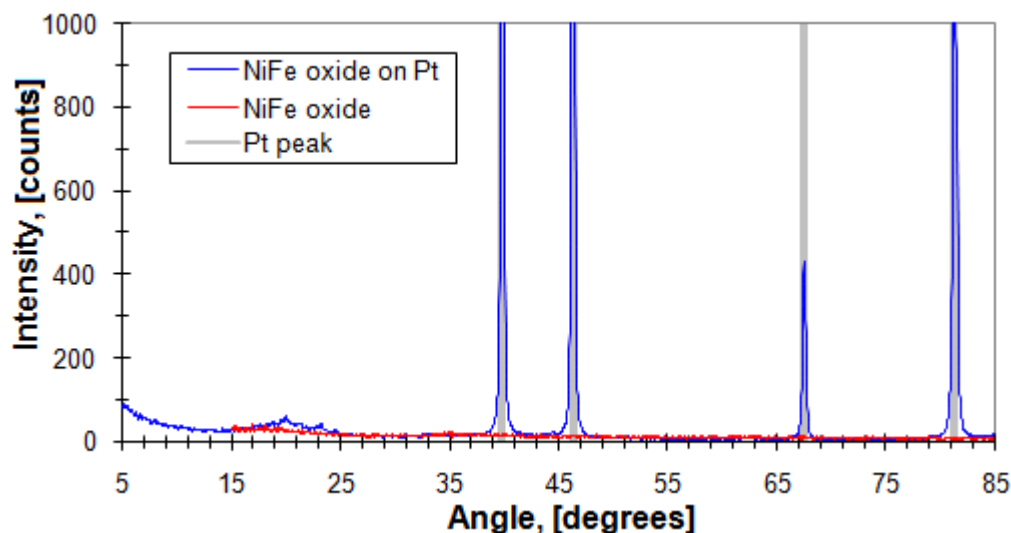


Figure 3.26: X-ray powder crystallography of the NiFe oxide with and without the platinum support.

3.5.2 X-ray powder crystallography

The NiFe oxide catalyst was analyzed with X-ray powder crystallography both with and without the platinum support (Figure 3.26). Only signals corresponding to metallic platinum were detected when the platinum support was present. No signals corresponding nickel or iron could be detected with the platinum support. The lack of any clear signals indicated that the crystal size for organized chemical structures was too small to be detected by X-ray diffraction of that the structure was amorphous.

3.5.3 X-ray photoelectron microscopy

The analysis of the NiFe oxide catalyst with XPS produced the Ni $2p^{3/2}$, Fe $2p^{3/2}$, and O $1s$ multiplets illustrated in Figures 3.28, 3.29, and 3.30, respectively. The XPS multiplets did not change significantly after a 5 minute sputtering with 1 KeV Argon ions at 200 nA stage. The XPS peaks encompassed all of the nickel or iron oxidation state binding energies available in the NIST database (<http://srdata.nist.gov/xps/>) except for the metallic states. The broad peaks indicated that all of the ionic nickel and iron oxidation states were incorporated in the NiFe oxide. The smoothness of the broad peaks indicated even distributions of energy states within the metal oxide structure.

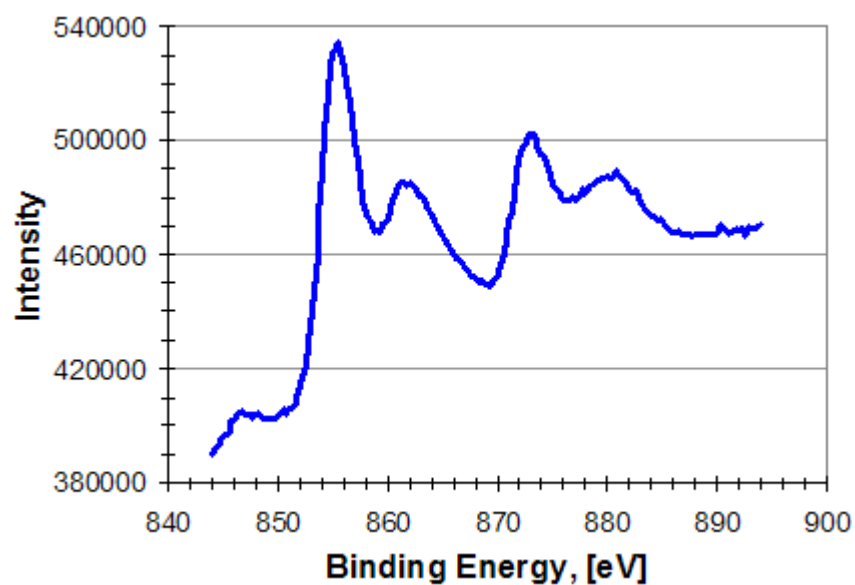


Figure 3.27: XPS Ni $2p^{3/2}$ multiplet of the NiFe oxide catalyst.

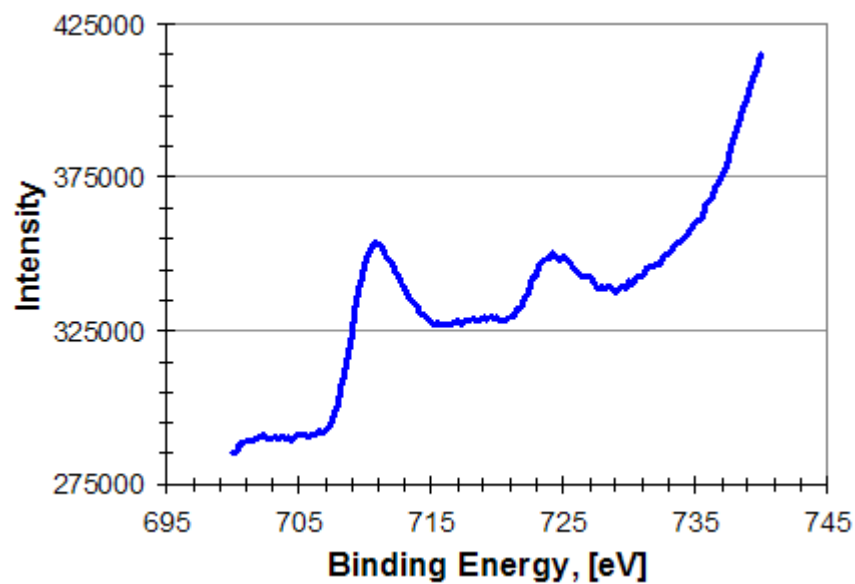


Figure 3.28: XPS Fe $2p^{3/2}$ multiplet of the NiFe oxide catalyst.

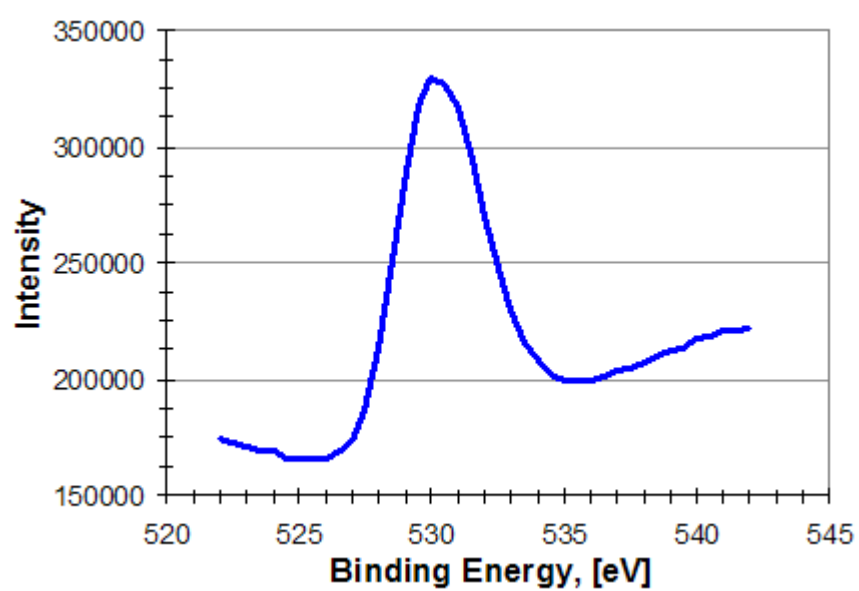


Figure 3.29: XPS O 1s multiplet of the NiFe oxide catalyst.

CHAPTER 4

CONCLUSIONS

4.1 Creating the catalysts

Observation of nature’s catalysis of the oxygen evolution and oxygen reduction reactions provided the successful foundation of this work. The analysis of photosystem II and cytochrome C oxidase indicated that metal oxides ranging from Mn to Cu would yield the best oxygen evolution catalysts. The systematic optimization of first row transition metal oxides resulted in NiFe oxide catalysts that demonstrated greater than 99 % ideal charge transfer coefficients for the alkaline oxygen evolution reaction and NiV oxide catalysts that demonstrated greater than 99.9 % ideal charge transfer coefficients for the alkaline hydrogen evolution reaction. A strong base was selected for the development and characterization of first-row transition metal oxide catalysts because these metal oxides are not chemically stable in acidic or sometimes even neutral electrolyte pH [3]. The purity of the H₂ and O₂ products were not measured because all other product reaction pathways were energetically unavailable. The hydroxyl radical, hydrogen peroxide, and hydrogen peroxy intermediates all have significantly higher potentials than molecular triplet-state oxygen product [13]. The potentials required for high current water oxidation with the catalysts developed in this work did not exceed the thermodynamic limit required for producing even hydrogen peroxy.

Figure 4.1 compares the sum of working potentials for the NiFe and NiV oxide catalytic kinetics illustrated in Figures 3.1 and 3.2 with the sum of working potentials for the hydrogen and oxygen evolution kinetics on the bare platinum support electrodes and the minimum power required for water electrolysis. Water electrolysis was performed at greater than 99 % efficiency below 10 mA/cm² with the use of the metal oxide catalysts developed in this work. Commercial alkaline electrolyzers range from 65–75 % efficiency [70]. Pure platinum was selected as a control because its efficiency for catalyzing water electrolysis is well known

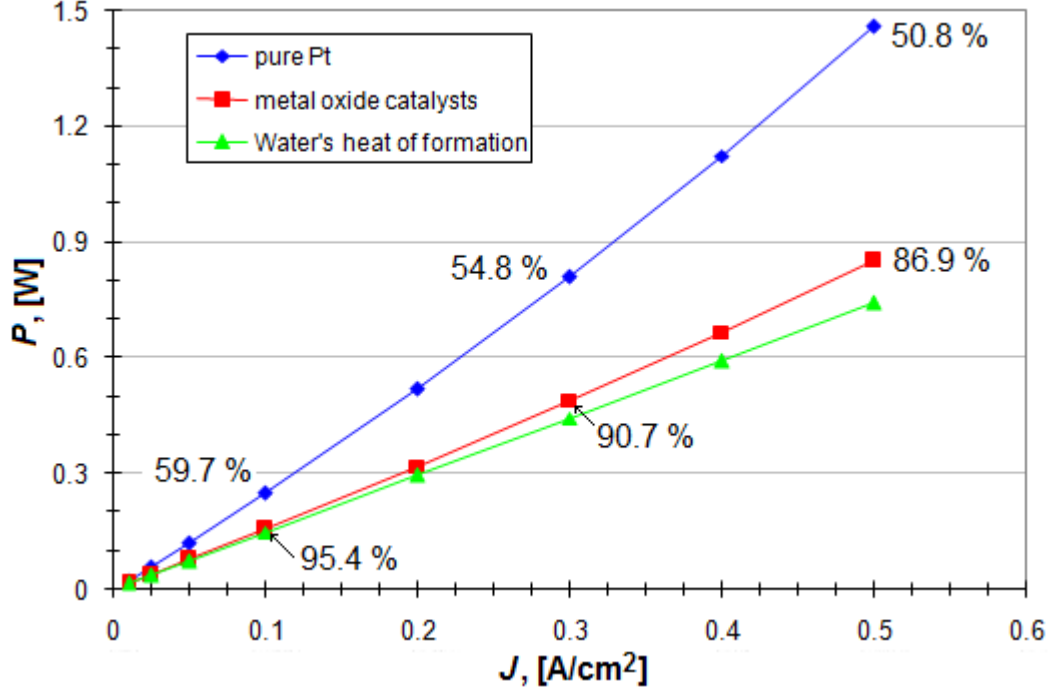


Figure 4.1: Power density, P , compared to current density, J , for the bare platinum support as both anode and cathode, for the NiFe and NiV oxide catalysts created by the high current electrodeposition method, and for water's heat of formation, ΔH in a 1 M KOH electrolyte.

and recyclable.

Metal oxide oxygen evolution catalysts created through cathodic electrodeposition demonstrated the best electron transfer coefficients in the surveyed literature. Prior work by Corrigan *et al.* on NiFe oxides created with cathodic electrodeposition techniques did not explore all of the electrodeposition variables. Catalytic performance of the NiFe oxide was optimized for oxygen evolution through exploration of buffer composition, buffer concentration, pH, metal ion concentration(s), metal ion oxidation state, metal salt counterion, current density, and current duration. It was discovered that kinetic performance was improved with the use of ammonium electrolytes to help the metal oxides deposit and the use of high current densities to form the catalysts. Corrigan reported Tafel slopes achieving 17 mV/decade current (slope K of Figure 1.8) whereas a slope of 14.8 mV/decade was reported in this work [33], [68]. The largest difference in kinetics was that Corrigan's catalysts had at least a 140 mV overvoltage at 1×10^{-5} A/cm² due to smaller J_0 values [33], [68]. A comparison of Tafel plots revealed similar slopes yet Corrigan's slope would be shifted ≥ 140

mV to higher (less efficient) potentials due to the larger NiFe J_0 values in this work.

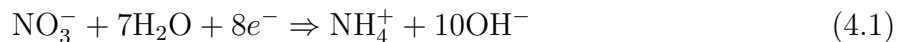
The electrodeposition method of catalyst formation was improved so that 1) the hydrogen and oxygen evolution catalysts demonstrated greater than 99 % ideal electron transfer efficiency, 2) efficiency was reproducible, and 3) the electrodeposition solutions could be reused to make multiple catalysts. The electrodeposition solutions could also be adjusted to contain only the metal ions, water, ammonium nitrate, and ammonium sulfate without significant effects upon the catalytic kinetics (Figure 3.7). Ammonium nitrate and ammonium sulfate are inexpensive ingredients of fertilizer. Remediation of the chemical wastes involved with producing these catalysts is expected to be simple and inexpensive.

The preparation of an electrodeposition solution, the synthesis of the catalyst through electrodeposition, and the kinetic characterization were quick and simple methods. Five undergraduates demonstrated the ability to prepare solutions, deposit catalysts, and then characterize the kinetics of five catalysts in less than 1.5 hours. Over 3,000 catalysts were created and kinetically characterized for this work. The trade-off for such a simple and expedient method of producing catalysts was the number of variables involved with the electrodeposition reaction that affected catalytic kinetics.

The formation of metal oxides from a reductive reaction may seem surprising because metal oxide formation is commonly associated with oxidation reactions. How can aqueous Ni^{2+} and Fe^{2+} ions form solid oxides from a reductive process? The addition of electrons to the metal ions themselves would produce nickel and iron alloys because neither metal is stable in the +1 oxidation state. The reductive processes of the cathodic electrodeposition reaction must have been associated with the solution's water molecules, spectator ions, or other non-transition metal electrolytes.

Corrigan proposed that the dissolved metal salt's anions, such as NO_3^- , decomposed in the cathode's electrolytic double layer according to reaction 4.1 [62], [63]. The decomposition of these anions produced a sufficient concentration of hydroxide ions in the double layer to precipitate the aqueous metal cations as solid hydroxides or hydrous oxides. Corrigan's proposed electrodeposition mechanism was not supported by experiments where Cl^- was the only anion present in the solution because the Cl^- anion could not undergo further reduction and therefore could not have produced a concentration of OH^- ions in the double layer. Electrodeposition solutions containing only NiCl_2 , FeCl_2 , and NH_4Cl produced efficient catalysts in this work (Figure 3.7). The cathodic decompositions of NO_3^- , SO_4^{2-} , and

ClO_4^- would yield various ratios of hydroxide ions produced per electron yet similar catalytic kinetics were observed for all three of these anions.



An alternative and novel mechanism for cathodic electrodeposition proposed here was based upon the reduction of water during electrodeposition because the high currents applied during electrodeposition required voltages far in excess of water's electrochemical domain of stability and substantial bubble formation was always present during deposition. For example, approximately 40 volts are required for a 250 mA/cm² electrodeposition of catalysts onto a 20 cm² working electrode with a 20 cm² counter electrode spaced 0.5 cm away from the working electrode. A combination of reactions 4.2 and 4.3 would produce both hydroxides and oxides to precipitate the metal cations. Greater electrodeposition current densities would favor reaction 4.3 over 4.2. The precipitation of metal ions by the reduction of water ligands would support the observations that harder spectator ions produced better catalytic kinetics and why other ligands that would displace water ligands, such as ethylene diamine and acetyl acetate, produced poorer catalytic kinetics.



4.2 Electrochemical characteristics

The electrochemical responses of the NiFe catalyst were characteristic of a conductive metal oxide. Electrical and ionic conductivity facilitate efficient electrocatalysis. Cyclic voltammetry experiments produced oscillation signals rather than peaks that would be caused by net oxidation or reduction. The high frequencies and large amplitudes observed in Figure 3.12 was evidence of highly mobile charged species [34]. The oscillations in current density were spontaneous because the oscillation frequencies observed in Figure 3.12 corresponded to the EIS frequency values (3.0–0.5 Hz) for negative real resistance ($-Z_R$) in the capacitive loops illustrated in Figure 3.15C. The conductivity of the metal oxides was also evident in the catalytic performance with unusually large exchange current density, J_0 , values.

The presence of a high frequency inductive loop was a unique characteristic of the metal oxide catalysts developed in this work in that it formed a loop, spanned from about 10^5 Hz to about 2×10^2 Hz, and was associated with negative resistance. Small values of inductance have been regularly observed in EIS of oxygen evolution catalysis and were usually dismissed as a result of the wiring in the electrochemical cell if the source was not reported as unknown [10], [42], [45], [47]. The inductive loop was not an artifact of the experimental setup because it did not appear for the electrode system without catalyst (Figure 3.15D).

Inductive behavior by metal oxide oxygen evolution catalysts has been previously reported for frequencies greater than 10^4 Hz and the “pseudo-inductance [was] associated with the disordered movement of charge carriers at the surface of the complex microstructure” [44]. High frequency inductance in combination with negative capacitance and negative resistance has also been theoretically explained and modeled to result from multi-electron transfer processes under biased conditions due to multiple species competing for adsorption sites [71]. The inductive loop observed in this work became increasingly disordered as catalysts switched from Butler-Volmer kinetics to resistive kinetics at higher working potentials.

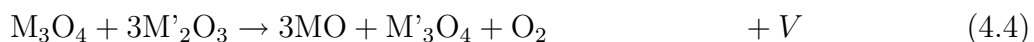
Analysis of the metal oxide catalysts proved difficult with conventional techniques. X-ray powder crystallography and X-ray photoelectron spectroscopy yielded little evidence concerning the catalytic mechanism. Electrochemical impedance spectroscopy proved useful for characterizing the oxides during catalysis because different half-reactions of different metals were active at different working potentials and frequencies. The reactions whose combination of potentials correlated with the phase angle’s approach to zero were used to construct the catalytic mechanism. The charge transfer resistance approached the limit of zero when the phase angle approached zero and the overpotential was greater than the activation energy. The catalyst composition determined the charge transfer resistance. The catalysts reached minimum resistance when the working potential was sufficient to simultaneously drive all of the reactions in the mechanism.

The proposed NiFe mechanism resembled previous work on Ni and other NiFe oxide oxygen evolution catalysts [33], [60], [61], [62], [63], [68]. The hydrated Ni_3O_4 state was suggested in oxygen evolution by Trivedi *et al.* [72]. Corrigan *et al.* presented evidence supporting the involvement of the hydrated NiO (also known as $\text{Ni}(\text{OH})_2$) in NiFe oxide catalytic cycles studied by angle-resolved infrared spectroelectrochemistry [65], surface-enhanced Raman scattering [60], and in situ surface Raman spectroscopy [63]. Corrigan

et al. also presented evidence supporting the involvement of hydrated Fe_2O_3 (FeOOH) in the catalytic mechanism with *in situ* Mössbauer spectroscopy [61]. The mechanistic information suggested by Corrigan *et al.* was different in that he suggested the presence of nickel in NiOOH (hydrated Ni_2O_3) [63] and tetra-valent states [62], [63], [66]. The Ni_2O_3 and quadric-valent nickel states were observed with XPS in this work (Figure 3.28) although the impedance technique did not indicate that the state actively participated in catalysis.

The validity of identifying half-reactions involved with the catalytic mechanism with impedance spectroscopy was supported by the trends in identified reactions. Two trends in the reactions and correlations emerged: 1) the phase angle correlated with reactions that only involve MO , M_3O_4 , or M_2O_3 oxidation states, 2) the correlations for combinations of individual half-reaction potentials only and always appeared when the individual half-reactions caused correlations. All three of these allowed oxidation states are only stable for Ni, Co, Fe, and Mn (photosystem II). Empirical optimization of first-row transition metal oxides for catalysis of the oxygen evolution reaction produced the best efficiencies when the catalyst contained Ni, Co, Fe, Mn, or combinations thereof. The detection of only reactions that included the M_3O_4 oxidation state of Mn, Fe, Co, or Ni was also consistent with the identification of the M_3O_4 oxidation state in the literature survey of alkaline oxygen evolution catalysts [10], [11], [14], [16], [17], [18], [22], [23], [53]. The MO_2 state was never correlated by impedance spectroscopy even though the state was also stable these metals. The transitions to and from the M_3O_4 mixed oxidation state may be responsible for facilitating the electron spin inversion.

The NiFe and CoFe mechanisms mirrored each other. The same set of oxidation states and transitions were present in the reactant and product sides of the mechanisms despite the substitution of nickel for cobalt. The NiFe and CoFe mechanisms both followed the format described by reaction 4.4 where the sum of the half-reaction potentials was spontaneous and M and M' may be different metal elements. The NiCo mechanism included two different sets of reaction 4.4 because the sum of potentials for the individual sets was not great enough to drive oxygen evolution. The combination of both sets was necessary for the NiCo mechanism to be spontaneous.



“It would be difficult to find more important topics in the whole of electrochemistry as

the anomalies of $[\alpha]$ ” [26]. Impedance data was correlated with the Butler-Volmer model of charge transfer by establishing the relationship of the charge transfer resistance, R_{ct} , with the electron transfer coefficient, α . This empirically developed relationship between R_{ct} and α was important for three reasons: 1) the relationship defined how the electrochemical workstation’s circuit, including the reference electrode, affected magnitude of measured impedance values, 2) the relationship identified how measured impedance values deviated from true impedance values at lower working potentials and how to correct for the deviation, and 3) introduced a means to analyze the time-dependant characteristics of charge transfer coefficients.

The measured impedance values deviated away from the true impedance values at lower current densities because the system of measuring the data is flawed. The electrochemical workstation only measured the impedance and phase angle of the positive peak of the sine waves as illustrated in Figure 2.1. Only the positive peak was measured because of the technique’s origin in analyzing electrical circuits because electrical circuits are linear systems. A linear increase in voltage produces a linear increase in current. The impedance and phase angle are equal and opposite for the positive and negative sine wave peaks in linear systems. Electrochemical systems are non-linear at lower current densities where the catalyst demonstrates Butler-Volmer kinetics. The impedance and phase angle are not equal and opposite for the positive and negative sine wave peaks in non-linear systems. The impedance values of non-linear systems will appear distorted when the catalytic system demonstrates Butler-Volmer kinetics (Figures 3.20, 3.21, 3.22) when only one of the two wave peaks is measured. Figure 4.2 illustrates how a 10 mV input wave amplitude is distorted by an ideal oxygen evolution Tafel slope (non-linear) in comparison with the average current density of that slope (linear).

Maxwell’s equations indicate that the electric and magnetic fields are orthogonal and $\pi/2$ out of phase for ideal energy transfer in time-dependant fields. The electric (ZR) and magnetic (ZI) impedances of a NiFe oxide catalyst are illustrated in Figure 4-3 with respect to frequency at 0.440 V. The electric and magnetic impedances were $\pi/2$ out of phase at four frequencies in the measured spectrum and were close to being $\pi/2$ out for the rest of the frequencies. Figure 4-4 provides a three-dimensional perspective of the electric and magnetic impedances with respect to frequency.

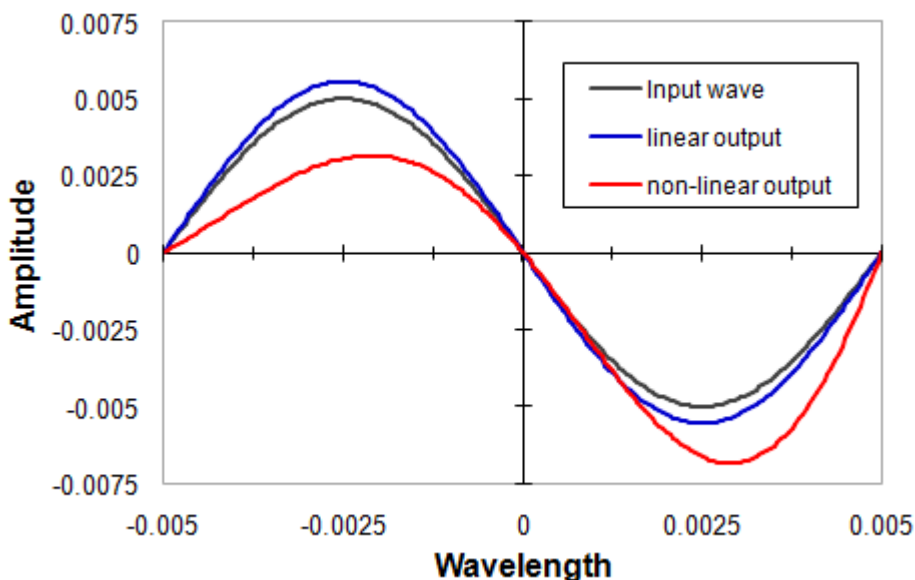


Figure 4.2: Wave distortion in linear and non-linear systems measured with a 10 mV input wave amplitude.

4.3 Catalystst chemical structure

Chemical reactivity is a function of the catalyst's chemical structure [34]. The development of catalysts has been retarded by the development of this structure/function relationship in a key way: well-defined atomic organizations at well-defined conditions are required for determining the chemical structure of the catalysts through analytical techniques. The role of defects in catalysts has been obscured in the pursuit of obtaining well-defined chemical structures [73]. The importance of defects in catalysis is re-emerging. The importance of the role of defects in other materials such as semiconductors, superconductors, gas sensors, oxygen pumps, etc., is emerging as a field of research known as defect chemistry.

The correlation of catalytic activity with structural defects was established in the 1920's and is being even more clearly established today [74], [75]. Merkle *et al.* provided an excellent recent survey of reactions in which catalytic defect chemistry was systematically varied and directly correlated with reaction rates [75]. Defects increase the range and density of energy states in a material and can be modeled by acid-base chemistry [75], [76], [77]. Defects in transition-metal oxides are known to cause electric and ionic conductivity and enable the transport of neutral oxygen atoms through the matrix [76]. Highly reactive catalysts are

expected to be highly defective and disordered.

X-ray powder crystallography and X-ray photoelectron microscopy yielded little information concerning the chemical structure of the NiFe catalyst because the metal oxide was so defective. The lack of any detectable signal in X-ray powder crystallography indicated that the metal oxide was polycrystalline with crystal sizes too small to be detected with a 0.154 nm wavelength or that the metal oxide was amorphous (Figure 3.26). X-ray photoelectron microscopy also indicated a disordered oxide because the peaks have been broadened by a distribution in the Madelung constants (Figures 3.28, 3.29, and 3.30). The metal oxides created from the high current cathodic electrodeposition technique are therefore considered to be highly defective materials. Corrigan also noted a difficulty in discerning structural information with regard to his NiFe oxide catalysts and turned to developing *in situ* Moössbauer and *in situ* surface enhanced Raman spectroscopy techniques [60], [61], [62].

APPENDIX A

Symbols, terms, and constants

Symbols, terms, and constants

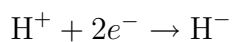
A	current (amp, ampere, C/s)
α	charge transfer coefficient
$\alpha(a)$	anodic charge transfer coefficient
$\alpha(c)$	cathodic charge transfer coefficient
C	Coulomb (C, F/N _A), 6.24 x 10 ¹⁸ e ⁻
C	capacitance (F , C/V)
C_d	differential capacitance (F , C/V)
$C_{d,e}$	external differential capacitance (F , C/V)
$C_{d,i}$	internal differential capacitance (F , C/V)
E	electric potential (V)
E_0	standard state potential
EIS	electrochemical impedance spectroscopy
e ⁻	electron, e ⁻ = 1.60218 x 10 ⁻¹⁹ C
F	Faradays constant, 9.6485 x 10 ⁴ C/mol
F	farad, (F , 1 C/V)
ΔG	change in free energy (kJ/mol)
ΔG_f	free energy of formation (kJ/mol)
ΔH	change in enthalpy (kJ/mol)
ΔH_f	heat of formation (kJ/mol)
Hz	Hertz (s ⁻¹)
I	current (A, C/s)
I_0	exchange current (A or mA)

J	Joule (J, C·V)
J	current density (A/cm ² or mA/cm ²)
J_0	exchange current density (A/cm ² or mA/cm ²)
K	Kelvin
K	standard state equilibrium constant
LVS	linear voltammetry scan
M	molecular weight (g/mol)
N_A	Avagadros number, $6.022 \times 10^{23} \text{ mol}^{-1}$
n	number of e ⁻ or mol
P	power (W, watt, $\frac{\text{C}\cdot\text{V}}{\text{s}}$)
q	charge (C)
θ	phase angle (radians or degrees)
R	gas law constant, $8.3145 \frac{\text{J}}{\text{mol}\cdot\text{K}}$
R	resistance (ohm, $\frac{\text{V}\cdot\text{s}}{\text{C}}$)
R_{ct}	charge transfer resistance
R_{mt}	mass transfer resistance
R_{soln}	solution resistance
ΔS	change in entropy ($\frac{\text{J}}{\text{mol}\cdot\text{K}}$)
s	second
SEM	scanning electron microscopy
T	temperature (°K)
V	volt (V, J/C)
ϕ	morphology factor, $\frac{C_{d,i}}{C_d}$
W	Watt (J/s, $\frac{\text{C}\cdot\text{V}}{\text{s}}$)
XPS	X-ray photoelectron spectroscopy
Z	impedance (ohm·cm ²)
Z_I	imaginary impedance (ohm·cm ²)
Z_R	real impedance (ohm·cm ²)

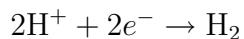
APPENDIX B

Reactions and Reduction Potentials

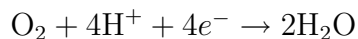
Reactions and Reduction Potentials [3]



$$E = -1.125 + 0.0295 \log \frac{\text{H}^+}{\text{H}^-}$$



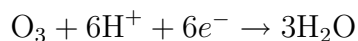
$$E = 0.000 - 0.0592 \cdot \text{pH} + 0.0295 \log(p\text{H}_2)$$



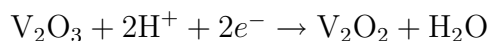
$$E = 1.228 - 0.0592 \cdot \text{pH} + 0.0147 \log(p\text{O}_2)$$



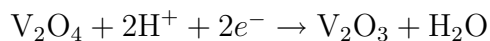
$$E = 1.362 - 0.0295 \cdot \text{pH} + 0.0295 \log(\text{H}_2\text{O}_2)$$



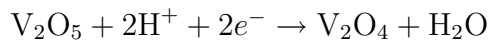
$$E = 1.501 - 0.0592 \cdot \text{pH} + 0.0098 \log(p\text{O}_3)$$



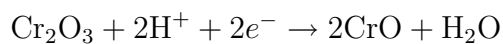
$$E = -0.549 - 0.0592 \cdot \text{pH}$$



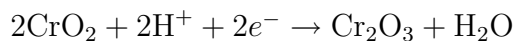
$$E = 0.210 - 0.0592 \cdot \text{pH}$$



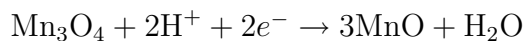
$$E = 0.708 - 0.0592 \cdot \text{pH}$$



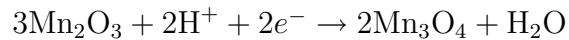
$$E = -0.785 - 0.0592 \cdot \text{pH}$$



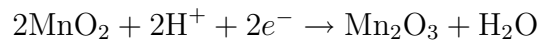
$$E = 1.284 - 0.0592 \cdot \text{pH}$$



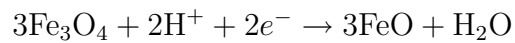
$$E = 0.462 - 0.0592 \cdot \text{pH}$$



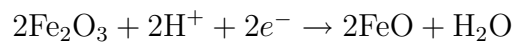
$$E = 2.014 - 0.0592 \cdot \text{pH}$$



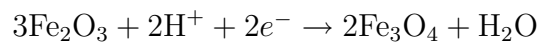
$$E = 0.573 - 0.0592 \cdot \text{pH}$$



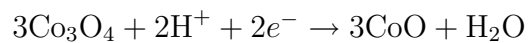
$$E = -0.197 - 0.0592 \cdot \text{pH}$$



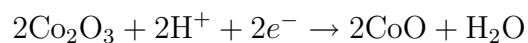
$$E = 0.271 - 0.0592 \cdot \text{pH}$$



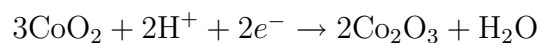
$$E = 1.208 - 0.0592 \cdot \text{pH}$$



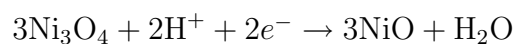
$$E = 0.993 - 0.0592 \cdot \text{pH}$$



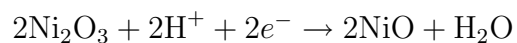
$$E = 1.018 - 0.0592 \cdot \text{pH}$$



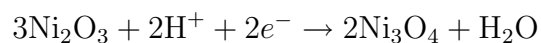
$$E = 1.477 - 0.0592 \cdot \text{pH}$$



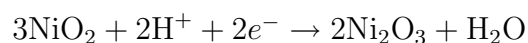
$$E = 0.897 - 0.0592 \cdot \text{pH}$$



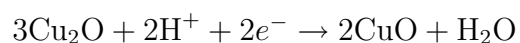
$$E = 1.023 - 0.0592 \cdot \text{pH}$$



$$E = 1.305 - 0.0592 \cdot \text{pH}$$



$$E = 1.434 - 0.0592 \cdot \text{pH}$$



$$E = 0.747 - 0.0592 \cdot \text{pH}$$

REFERENCES

- [1] D. L. Nelson and M. M. Cox. *Lehninger Principles of Biochemistry*. Worth Publishers, New York, 2000. [1.2](#)
- [2] M. Paumann, G. Regelsberger, and G. A. Peschek. The bioenergetic role of dioxygen and the terminal oxidase(s) in cyanobacteria. *Biochimica et Biophysica Acta*, 1707:231–253, 2005. [1.2](#), [1.6](#)
- [3] M. Pourbaix. *Atlas of Electrochemical Equilibria in Aqueous Solution*. Cebalcor, Brussels, 1974. [1.3](#), [3.4.1](#), [4.1](#), [B](#)
- [4] R. L. LeRoy, C. T. Bowen, and D. J. LeRoy. The thermodynamics of aqueous water electrolysis. *J. Electrochem. Soc.*, 27(9):1954–1962, 1980. [1.3](#)
- [5] K. Onda, T. Kyakuno, K. Hattori, and K. Ito. Prediction of production power for high-pressure hydrogen by high-pressure water electrolysis. *Journal of Power Sources*, 132:64–70, 1980. [1.3](#)
- [6] A. Roy, S. Watson, and D. Infield. Comparison of electrical energy efficiency of atmospheric and high pressure electrolyzers. *International Journal of Hydrogen Energy*, 31:1964–1979, 2006. [1.3](#)
- [7] D. C. Harris. *Quantitative Chemical Analysis*. W. H. Freeman and Company, New York, 1999. [1.4](#)
- [8] D. M. See and R. E. White. Temperature and concentration dependence of the specific conductivity of concentrations of potassium hydroxide. *J. Chem. Eng. Data*, 42:1266–1268, 1997. [1.4](#)
- [9] E. Rodil, K. Persson, J. H. Vera, and G. Wilczek-Vera. Determination of the activity of H^+ ions within and beyond the pH meter range. *AIChE Journal*, 47(12):2807–2818, 2001. [1.4](#), [2.2](#)
- [10] R. N. Singh, N. K. Singh, and J. P. Singh. Electrocatalytic properties of new active ternary ferrite film anodes for O_2 evolution in alkaline medium. *Electrochimica Acta*, 47:3873–3879, 2002. [1.4](#), [1.7](#), [4.2](#)
- [11] M. I. Godinho, M. A. Catarino, M. I. da S. Pereira, M. H. Mendonca, and F. M. Costa. Effect of partial replacement of Fe by Ni and/or Mn on the electrocatalytic activity for oxygen evolution of the CoFe_2O_4 spinel oxide electrode. *Electrochimica Acta*, 47:4307–4314, 2002. [1.4](#), [1.7](#), [4.2](#)

- [12] C. C. Hu and Y. R. Wu. Bipolar performance of the electroplated iron-nickel deposits for water electrolysis. *Materials Chemistry and Physics*, 82:588–596, 2003. [1.4](#), [1.7](#)
- [13] G. L. Elizarova, G. M. Zhidomirov, and V. N. Parmon. Hydroxides of transition metals as artificial catalysts for oxidation of water to dioxygen. *Catalysis Today*, 58:71–88, 2000. [1.4](#), [1.7](#), [4.1](#)
- [14] M. P. Elizalde, M. Gonzalez, E. Garcia, M. M. Davila, and G. Poillerat. Characterization of ni-polyvinylchloride and nico₂o₄/ni-polyvinylchloride composites as electrodes in alkaline solutions. *J. Electrochem. Soc.*, 144(9):263–266, 1997. [1.4](#), [1.7](#), [4.2](#)
- [15] E. L. Miller and R. E. Rocheleau. Electrochemical behavior of reactively sputtered iron-doped nickel oxide. *J. Electrochem. Soc.*, 144(9):3072–3077, 1997. [1.4](#), [1.7](#)
- [16] J. Ponce, E. Rios, J. L. Rehspringer, G Poillerat, P. Chartier, and J. L. Gautier. Preparation of nickel aluminum-manganese spinel oxides nixa1-xmn₂o₄ for oxygen electrocatalysis in alkaline medium: comparison of properties stemming from different preparation methods. *Journal of Solid State Chemistry*, 145:23–32, 1999. [1.4](#), [1.7](#), [4.2](#)
- [17] J. Ponce, J. L. Rehspringer, G Poillerat, and J. L. Gautier. Electrochemical study of nickel-aluminum-manganese spinel nixa1-xmn₂o₄. electrocatalytical properties for the oxygen evolution reaction and oxygen reduction reaction in alkaline media. *Electrochemica Acta*, 46:3373–3380, 2001. [1.4](#), [1.7](#), [4.2](#)
- [18] V. Rashkova, S Kitova, I. Konstantinov, and T. Vitanov. Vacuum evaporated thin films of mixed cobalt and nickel oxides as electrocatalysts for oxygen evolution and reduction. *Electrochemica Acta*, 47:1555–1560, 2002. [1.4](#), [1.7](#), [4.2](#)
- [19] A. Kahoul, A. Hammouche, F. Naamoune, P. Chartier, G. Poillerat, and J. F. Keonig. Solvent effect on synthesis of perovskite-type la_{1-x}ca_xcoo₃ and their electrochemical properties for oxygen reactions. *Materials Research Bulletin*, 35:1955–1966, 2000. [1.4](#), [1.7](#)
- [20] A. Kahoul, A. Hammouche, G. Poillerat, and R. W. de Donker. Electrocatalytic activity and stability of la_{1-x}ca_xcoo₃ perovskite-type oxides in alkaline medium. *Catalysis Today*, 89:287–291, 2004. [1.4](#), [1.7](#)
- [21] V. A. Alves, L. A. da Silva, and J. F. C. Boodts. Surface characterization of iro₂/tio₂/ceo₂ oxide electrodes and faradaic impedance investigation of the oxygen evolution reaction from alkaline solution. *Electrochemica Acta*, 44:1525–1534, 1998. [1.4](#), [1.7](#)
- [22] M. H. Mendonca, M. I. Godinho, M. A. Catarino, M. I. da S. Periera, and F. M. Costa. Preparation and characterization of spinel oxide ferrites suitable for oxygen evolution anodes. *Solid State Sciences*, 4:175–182, 2002. [1.4](#), [1.7](#), [4.2](#)
- [23] E. Rios, Y. Y. Chen, M. Gracia, J. F. Marco, J. R. Gancedo, and J. L. Gautier. Influence of the partial replacement of fe by mn on the electrocatalytic activity for

- oxygen evolution in the $\text{Li}(1 - 0.5x)\text{Fe}(1.5x + 1)\text{Mn}(1 - x)\text{O}_4$ spinel system. *Electrochimica Acta*, 47:559–566, 2002. [1.4](#), [1.7](#), [4.2](#)
- [24] N. Nagai, M. Takeuchi, and T. Oka. Existence of optimum space between electrodes on hydrogen production by water electrolysis. *International Journal of Hydrogen Energy*, 28:35–41, 2003. [1.4](#)
- [25] L. M. da Silva, L. A. de Faria, and J. F. C. Boodts. Determination of the morphology factor of oxide layers. *Electrochimica Acta*, 47:395–403, 2001. [1.4](#), [2.5](#), [3.3](#)
- [26] J. O’M. Bockris and S. U. M. Khan. *Surface Electrochemistry: A Molecular Level Approach*. Plenum Press, New York, 1993. [1.5](#), [1.6](#), [1.7](#), [4.2](#)
- [27] R. Poli and J. N. Harvey. Spin forbidden reactions of transition metal compounds. new ideas and new computational challenges. *Chem. Soc. Rev.*, 32:1–8, 2003. [1.6](#)
- [28] H. A. Gasteiger, S. S. Kocha, B. Sompalli, and F. T. Wagner. Activity benchmarks and requirements for Pt, Pt-alloy, and non-Pt oxygen reduction catalysts for PEMFCs. *Applied Catalysis B: Environmental*, 56:9–35, 2005. [1.6](#)
- [29] R. J. Pace and K. A. Ahrling. Water oxidation in psiih atom abstraction revisited. *Biochem. Biophys.*, 1655:172–178, 2004. [1.6](#)
- [30] B. Schmidt, W. Hillier, J. McCracken, and S. Ferguson-Miller. The use of stable isotopes and spectroscopy to investigate the energy transducing function of cytochrome c oxidase. *Biochem. Biophys.*, 1655:248–255, 2004. [1.6](#)
- [31] B. N. Figgis and M. A. Hitchman. *Ligand Field Theory and Its Applications*. Wiley-VCH, New York, 2000. [1.6](#)
- [32] G. Halpert. Past developments and future of nickel electrode cell technology. *Journal of Power Sources*, 12(3-4):177–192, 1984. [1.6](#)
- [33] D. A. Corrigan. The catalysis of the oxygen evolution reaction by iron impurities in thin film nickel oxide electrodes. *J. Electrochem. Soc.*, 134(2):377–384, 1987. [1.6](#), [1.7](#), [4.1](#), [4.2](#)
- [34] R. A. Van Santen. Catalysis: closing the molecular and macroscopic sciences gap. *Chemical Engineering Science*, 50(24):4027–4044, 1995. [1.6](#), [4.2](#), [4.3](#)
- [35] J. M. Caruthers, J. A. Lauterbach, K. T. Thomson, V. Venkatasubramanian, C. M. Snively, A. Bhan, S. Katare, and G. Oskarsdottir. Catalyst design: knowledge extraction from high-throughput experimentation. *Journal of Catalysis*, 216:98–109, 2003. [1.6](#)
- [36] A. Hellman, E. J. Baerends, M. Biczysko, T. Bligaard, C. H. Christensen, D. C. Clary, S. Dahl, R. van Harrevelt, K. Honkala, H. Jonsson, G. J. Kroes, M. Luppi, U. Manthe, J. K. Nørskov, R. A. Olsen, J. Rossmeisl, E. Skúlason, C. S. Tautermann, A. J. C. Varandas, and J. K. Vincent. Predicting catalysis: understanding ammonia synthesis from first-principles calculations. *J. Phys. Chem.*, 110:17719–17735, 2006. [1.6](#)

- [37] A. Corma, J. M. Serra, P. Serna, and M. Moliner. Integrating high-throughput characterization into combinatorial heterogeneous catalysis: unsupervised construction of quantitative structure/property relationship models. *Journal of Catalysis*, 232:335–341, 2005. [1.6](#)
- [38] L. A. Baumes, J. M. Serra, P. Serna, and A. Corma. Support vector machines for predictive modeling in heterogeneous catalysis: a comprehensive introduction and overfitting investigation based on two real applications. *J. Comb. Chem.*, 8:583–596, 2006. [1.6](#)
- [39] C. Tabares-Mendoza and P. Guadarrama. Predicting the catalytic efficiency by quantum-chemical descriptors: theoretical study of pincer metallic complexes involved in the catalytic heck reaction. *Journal of Organometallic Chemistry*, 691:2978–2986, 2006. [1.6](#)
- [40] A. de Oliveria-Sousa, M. A. S. da Silva, S. A. S. Machado, L. A. Avaca, and P. de Lima-Neto. Influence of the preparation method on the morphological and electrochemical properties of ti/iro2-coated electrodes. *Electrochimica Acta*, 45:4467–4473, 2000. [1.7](#)
- [41] J. Prakash, D. A. Tryk, and E. B. Yeager. Kinetic investigations of oxygen reduction and evolution on lead ruthenate catalysts. *J. Electrochem. Soc.*, 146(11):4145–4151, 1999. [1.7](#)
- [42] A. J. Terezo, J. Bisquert, E. C. Pereira, and G. Garcia-Belmonte. Separation of transport, charge storage and reaction processes of porous electrocatalytic iro2 and iro2/nb2o5 electrodes. *Journal of Electroanalytical Chemistry*, 508:59–69, 2001. [1.7](#), [4.2](#)
- [43] F. I. Mattos-Costa, P. de Lima-Neto, S. A. S. Machado, and L. A. Avaca. Characterization of surfaces modified by sol-gel derived ruxir1 xo2 coatings for oxygen evolution in acidic medium. *Electrochimica Acta*, 44:1515–1523, 1998. [1.7](#)
- [44] L. M. da Silva, K. C. Fernandes, L. A. de Faria, and J. F. C. Boodts. Electrochemical impedance spectroscopy study during accelerated life test of conductive oxides: Ti/(ru + ti + ce)o2-system. *Electrochimica Acta*, 49:4893–4906, 2004. [1.7](#), [4.2](#)
- [45] J. M. Hu, J. Q. Zhang, and C. N. Cao. Oxygen evolution on iro2-based dsa type electrodes: kinetics analysis of tafel lines and eis. *International Journal of Hydrogen Energy*, 29:791–797, 2004. [1.7](#), [4.2](#)
- [46] A. Rossi and J. F. C. Boodts. Ir-based oxide electrodes: oxygen evolution reaction from mixed solvents. *Journal of Applied Electrochemistry*, 32:735–741, 2002. [1.7](#)
- [47] L. A. da Silva, V. A. Alves, M. A. P. da Silva and S. Trasatti, and J. F. C. Boodts. Oxygen evolution in acidic solution on iro2 +tio2 ceramic films. a study by impedance, voltammetry and sem. *Electrochimica Acta*, 42(2):271–281, 1997. [1.7](#), [4.2](#)
- [48] M. Bursell, M. Pirjamali, and Y. Kiros. La0.6ca0.4coo3, la0.1ca0.9mno3 and lanio3 as bifunctional oxygen electrodes. *Electrochimica Acta*, 47:1651–1660, 2002. [1.7](#)

- [49] R. Bertoncello, S. Cattarin, I. Frateur, and M. Musiani. Preparation of anodes for oxygen evolution by electrodeposition of composite oxides of pb and ru on ti. *Journal of Electroanalytical Chemistry*, 492:145–149, 2000. [1.7](#)
- [50] L. M. da Silva, J. F. C. Boodts, and L. A. Faria. Oxygen evolution at $\text{ruo}_2(\text{x}) + \text{co}_3\text{o}_4(1-\text{x})$ electrodes from acid solution. *Electrochimica Acta*, 46:1369–1375, 2001. [1.7](#)
- [51] C. Baruffaldi, S. Cattarin, and M. Mussiani. Deposition of non-stoichiometric tungsten oxides + mo_2 composites ($\text{m} = \text{ru}$ or ir) and study of their catalytic properties in hydrogen or oxygen evolution reactions. *Electrochimica Acta*, 48:3921–3927, 2003. [1.7](#)
- [52] M. Musiani, F. Furlando, and R. Bertoncello. Electrodeposited $\text{pbo}_2 + \text{ruo}_2$: a composite anode for oxygen evolution from sulfuric acid solution. *Journal of Electroanalytical Chemistry*, 465:160–167, 1999. [1.7](#)
- [53] S. Cattarin, P. Guerriero, and M. Musiani. Preparation of anodes for oxygen evolution by electrodeposition of composite pb and co oxides. *Electrochimica Acta*, 46:4229–4234, 2001. [1.7](#), [4.2](#)
- [54] K. Izumiya, E. Akiyama, H. Habazaki, A. Kawashima, and K. Hashimoto. Anodically deposited manganese oxide and manganese-tungsten oxide electrodes for oxygen evolution from seawater. *Electrochimica Acta*, 43:3303–3312, 1998. [1.7](#)
- [55] N. A. Abdel Ghany, N. Kumagai, S. Meguro, K. Asami, and K. Hashimoto. Oxygen evolution anodes composed of anodically deposited mn-mo-fe oxides for seawater electrolysis. *Journal of Electroanalytical Chemistry*, 48:21–28, 2002. [1.7](#)
- [56] H. Habazaki, H. Matsui, A. Kawashima, K. Asami, N. Kumagai, and K. Hashimoto. Nanocrystalline manganese-molybdenum-tungsten oxide anodes for oxygen evolution in seawater electrolysis. *Scripta mater.*, 44:1659–1662, 2001. [1.7](#)
- [57] T. Matsui, H. Habazaki, A. Kawashima, K. Asami, N. Kumagai, and K. Hashimoto. Anodically deposited manganese-molybdenum-tungsten oxide anodes for oxygen evolution in seawater electrolysis. *Journal of Applied Electrochemistry*, 32:93–100, 2002. [1.7](#)
- [58] K. Fujimura, T. Matsui, H. Habazaki, A. Kawashima, N. Kumagai, and K. Hashimoto. The durability of manganese-molybdenum oxide anodes for oxygen evolution in seawater electrolysis. *Electrochimica Acta*, 45:2297–2303, 2000. [1.7](#)
- [59] K. Izumiya, E. Akiyama, H. Habazaki, A. Kawashima, K. Asimi, K. Hashimoto, and N. Kumagai. Surface activation of manganese oxide electrode for oxygen evolution from seawater. *Journal of Applied Electrochemistry*, 27:1362–1368, 1997. [1.7](#)
- [60] J. Desilvestro, D. A. Corrigan, and M. J. Weaver. Spectroelectrochemistry of thin nickel hydroxide films on gold using surface enhanced raman spectroscopy. *J. Phys. Chem.*, 90:6408–6411, 1986. [1.7](#), [4.2](#), [4.3](#)

- [61] D. A. Corrigan, R. S. Conell, C. A. Fierro, and D. A. Scherson. In situ mossbauer study of redox processes in a composite hydroxide of iron and nickel. *J. Phys. Chem.*, 91:5009–5011, 1987. [1.7](#), [4.2](#), [4.3](#)
- [62] J. Desilvestro, D. A. Corrigan, and M. J. Weaver. Characterization of redox states of nickel hydroxide film electrodes by in situ surface raman spectroscopy. *J. Electrochem. Soc.*, 135(4):885–892, 1988. [1.7](#), [4.1](#), [4.2](#), [4.3](#)
- [63] D. A. Corrigan and R. M. Bendart. Effect of coprecipitated metal ions on the electrochemistry of nickel hydroxide thin films: Cyclic voltammetry in 1 m koh. *J. Electrochem. Soc.*, 136(3):723–728, 1989. [1.7](#), [4.1](#), [4.2](#)
- [64] R. M. Bendart and D. A. Corrigan. Effect of coprecipitated metal ions on the electrochromic properties of nickel hydroxide. *J. Electrochem. Soc.*, 136(5):1369–1374, 1989. [1.7](#)
- [65] G. Nazri, D. A. Corrigan, and S. P. Maheswari. Angle-resolved infrared spectroelectrochemistry. 1. an in situ study of thin-film nickel oxide electrodes. *Langmuir*, 5:17–22, 1989. [1.7](#), [4.2](#)
- [66] M. L. Carpenter and D. A. Corrigan. Photoelectrochemistry of nickel hydroxide thin films. *J. Electrochem. Soc.*, 4:1022–1026, 1989. [1.7](#), [4.2](#)
- [67] J. L. Fernandez, M. R. de Chilvo, and A. C. Chilvo. Preparation and electrochemical characterization of ti/ruxmn1-xo2 electrodes. *Journal of Applied Electrochemistry*, 32:513–520, 2002. [1.7](#)
- [68] D. A. Corrigan. Hydrogen generator having a low oxygen overpotential electrode. *United States Patent*, Patent Number: 4,882,024, Date of Patent: Nov. 21 1989. [1.7](#), [4.1](#), [4.2](#)
- [69] W. S. Broeker. *How to Build a Habitable Planet*. Eldigo Press, New York, 2002. [2.2](#)
- [70] F. De Bruijn. The current status of fuel cell technology for mobile and stationary applications. *Green Chem.*, 7:132–150, 2005. [4.1](#)
- [71] B. Boukamp. Interpretation of an inductive loop in the impedance of an oxygen ion conducting electrolyte/metal electrode system. *Solid State Ionics*, 143:47–55, 2001. [4.2](#)
- [72] I. Arulraj and D. C. Trivedi. Characterization of nickel oxyhydroxide based anodes for alkaline water electrolysis. *J. Hydrogen Energy*, 14(12):893–898, 1989. [4.2](#)
- [73] A. B. Lidiard. 70 years of defect physical chemistry. *Phys. Chem. Chem. Phys.*, 5:2161–2163, 2003. [4.3](#)
- [74] I. M. Kolesnikov. Theory of catalysis of polyhedrons as the basis for investigation and selection of catalysts. *Chemistry and Technology of Fuels and Oils*, 41(2):120–130, 2005. [4.3](#)
- [75] R. Merkle and J. Maier. 70 years of defect physical chemistry. *Phys. Chem. Chem. Phys.*, 38:141–145, 2006. [4.3](#)

- [76] M. H. R. Lankhorst, H. J. M. Bouwmeester, and H. Verweij. Thermodynamics and transport of ionic and electronic defects in crystalline oxides. *Phys. Chem. Chem. Phys.*, 80(9):2175–2198, 1997. [4.3](#)
- [77] J. Maier. Point defects as acid-base active particles in ionic crystals. *Z. Anorg. Allg. Chem.*, 630:2562–2568, 2004. [4.3](#)

BIOGRAPHICAL SKETCH

Matthew D. Merrill

Matthew D. Merrill was born August 30, 1980 in Altadena, California.

In winter 2003, Matt completed his B.S. in Biology with Biochemistry and Chemistry minors and a concentration in Microbiology. He performed three years of undergraduate research on amylase enzymes in *Arabidopsis t*, none of it was successful however he learned a lot on how to deal with unsuccessful experiments. The undergraduate research was gratefully performed under the advisement and guidance of Dr. Jon Monroe.

Matt began the Department of Chemistry and Biochemistry's Ph.D. program at Florida State University in the summer of 2003 and completed in Winter 2007. He began working on water electrolysis catalysts in the Fall of 2004 under the advisement and guidance of Dr Ralph Dougherty and in collaboration with Dr Anjaneyulu Krothapali and Dr Brent Greska.

Matt's research interests include electrocatalysis, enzymatic catalysis, photocatalysis, electron transfer characterization, electrochemical impedance spectroscopy, and metabolism.

Matt currently lives in Tallahassee, Fl with his lovely wife Dani and with their two kitties, Boo and Wink.